

# Broadband Ground Motion Synthesis by Diffusion Model with Minimal Condition\*

Jaheun Jung<sup>†</sup>, Jaehyuk Lee<sup>†</sup>, Chang-Hae Jung, Hanyoung Kim, Bosung Jung, Donghun Lee<sup>‡</sup>

Department of Mathematics, Korea University  
145, Anam-ro, Seongbuk-gu, Seoul, Republic of Korea  
{wodsos, jaehyeokbear, changhae08, pinga999, 2018160026, holy}@korea.ac.kr

## Abstract

Earthquakes are rare. Hence there is a fundamental call for reliable methods to generate realistic ground motion data for data-driven approaches in seismology. Recent GAN-based methods fall short of the call, as the methods either require special information such as geological traits or generate sub-par waveforms that fail to satisfy seismological constraints such as phase arrival times. We propose a specialized Latent Diffusion Model (LDM) that reliably generates realistic waveforms after learning from real earthquake data with minimal conditions: location and magnitude. We also design a domain-specific training method that exploits the traits of earthquake dataset: multiple observed waveforms time-aligned and paired to each earthquake source that are tagged with seismological metadata comprised of earthquake magnitude, depth of focus, and the locations of epicenter and seismometers. We construct the time-aligned earthquake dataset using Southern California Earthquake Data Center (SCEDC) API, and train our model with the dataset and our proposed training method for performance evaluation. Our model surpasses all comparable data-driven methods in various test criteria not only from waveform generation domain but also from seismology such as phase arrival time, GMPE analysis, and spectrum analysis. Our result opens new future research directions for deep learning applications in seismology.

## Introduction

Broadband ground motion by seismic waves is crucial in the study of earthquakes and geology, since it includes important features related to subsurface structures of the Earth. At the same time, it is a great challenge from signal processing perspective, since observed ground motion time series data are noisy, covers a wide frequency band, and caused by rare and unevenly distributed earthquake events.

Various seismological applications were constructed by analyzing historically observed seismic waveforms. For example, as systematically recorded seismic waveform dataset grew, the accuracy of earthquake analysis were improved, early warning systems for earthquake-prone areas were polished, and earthquake-resistant architectural designs became more robust. In recent years, there has been significant

success in applying deep learning in seismology (Mousavi and Beroza 2022), such as seismic signal denoising (Zhu, Mousavi, and Beroza 2019), fault recognition (An et al. 2021), and earthquake event detection (Mousavi et al. 2020; Saad et al. 2023).

However, the field still faces a shortage of data, particularly for large-scale earthquakes (Shi et al. 2024; Katsanos, Sextos, and Manolis 2010). Recently, deep-learning based synthesis of seismic waveforms has emerged as a potential solution, mostly employing GAN-based generative models conditioned with various geological information and seismological desiderata (Wang, Trugman, and Lin 2021; Florez et al. 2022; Li et al. 2024; Chen, Li, and Guo 2024). However, the synthesized waveforms often lacks seismological realism, such as phase arrival times and amplitude of ground motion, especially when conditioning information is not reliable. We perceive this problem as an artifact of conditioned generation analogous to what GAN based models were suffering in image generation. Hence, we consider adaptation of diffusion models (Sohl-Dickstein et al. 2015; Ho, Jain, and Abbeel 2020) to seismic waveform data, in order to generate seismologically realistic ground motion waveforms with minimal condition.

## Our Contribution

- We design a diffusion model for seismic waveform synthesis, which requires a minimal set of conditional information comprised of magnitude and location of hypocenter and observation station.
- We propose a training framework that allows us to efficiently learn the seismic features from multiple observations of earthquake events.
- We construct a new evaluation dataset from an openly available seismic dataset (SCEDC), such that the observations are paired, with each pair coming from the same earthquake and aligned to the earthquake’s origin time.
- We demonstrate the effectiveness of the our generative model against benchmark models in various perspectives including domain-specific metrics such as GMPE and quantitative analysis on phase arrival times.

\*submitted to AAAI 2025, August 15, 2024

<sup>†</sup>These authors contributed equally.

<sup>‡</sup>corresponding author

## Problem Statement

Our goal is to generate the broadband ground motion data of seismic waves caused by existing earthquakes and observed at arbitrary locations, with high level of seismological realism, but without hard-to-obtain conditional information.

We consider this seismic waveform synthesis problem as conditional generation problem, which can be solved by data-driven methods with deep learning. Avoiding dependency on expensive-to-measure information, we define the following variables as the minimal condition for generation:

1.  $s_{lat}, s_{lon}$  : latitude and longitude of the station to observe the waveform data.
2.  $e_{lat}, e_{lon}$  : latitude and longitude of epicenter.
3.  $e_{dep}$  : depth of the hypocenter, unit of kilometers.
4.  $e_m$  : magnitude of the earthquake.

The above conditional information is usually considered to be insufficient for the ground motion synthesis, since seismological characteristics of earthquake such as focal mechanism or local geological characteristics of target site such as  $V_{S30}$  are not included. Instead of providing expensive additional information on earthquake, we suggest learning by waveform data directly, including the location information. To achieve this, we limit the region of interest, encode the latitude and longitude information of station and epicenter to local coordinates and learn the relation between location and waveform with hidden local features. Under these constraints, we construct a deep-learning-based generative method with *minimal condition* for seismic waveforms.

## Seismic Dataset

Seismic observations, comprising waveform data recorded by seismometers, possess distinct characteristics. Depending on the seismometer’s configuration, earthquake signals are captured in a specific format and at a defined sampling rate, typically classified as acceleration, velocity, or displacement. These seismograms contain vital information about the earthquake; for instance, the arrival times of P waves and S waves can be used to determine the epicentral distance and the depth of the hypocenter, while the waveform amplitude correlates with the earthquake’s magnitude.

However, seismic observations often include ambient noise from the surrounding environment and may be influenced by local geological conditions, which affect the accuracy of the data. As a result, seismic datasets exhibit unique properties, being a compilation of multiple noisy recordings of the same source, and the observed waveforms collectively retain the essential characteristics of the earthquake.

In this study, we take advantage of the property of seismic dataset that the multiple datapoints can be paired with a single earthquake. The paired observations would share properties of the same source earthquake, and hence generating one from another would be easier. For implementation, we select earthquakes since 2016 from the earthquake catalog of SCEDC dataset provided by SeisBench (Woolam et al. 2022), and collect waveform and corresponding metadata including locations, earthquake ID, magnitude and

P/S arrival time. We split the collected raw data for training and evaluation with respect to earthquake ID. Removing the datum with unknown seismic instrument response, total 89,366 traces are collected through 2,623 earthquakes and 149 stations. After raw dataset collection, we trim the waveform to have a duration of 60 seconds and apply detrend and bandpass filter (1 ~ 45Hz) sequentially. More details can be found in Appendix B.

During the training, we sample two paired waveforms ( $W^{tgt}, W^{src}$ ) from the dataset, which are distinct observations of same earthquake, and construct conditional vector  $\vec{c}_{tgt}$  from metadata by pre-processing stage, whose details are explained in Appendix A. In the next section, we explain how the waveforms are used to train the diffusion model.

## Method

Our approach builds on a music generation method (Ghosal et al. 2023) that initially creates spectrograms with its generative model and convert them into waveforms. We adapt the base model and construct a specialized training method to learn from the paired seismic waveform dataset.

### Diffusion Model Training with Paired Data

For each earthquake event, we sample a pair of waveforms ( $W^{src}, W^{tgt}$ ) from dataset and convert it to spectrograms ( $X^{src}, X^{tgt}$ ) and construct conditional vector of target station  $\vec{c}_{tgt}$  by preprocessing.

Let  $q(x_{1:T}; X)$  be the forward process of the diffusion model, and consider two trajectories  $q(x_t^{src} | X^{src})$  and  $q(x_t^{tgt} | X^{tgt})$ . Recall that  $X^{src}$  and  $X^{tgt}$  shares the property of earthquake, we may assume that from  $X^{src}$  and  $\vec{c}_{tgt}$  we can gather enough features of earthquake to generate  $X^{tgt}$ . In this approach, we may consider the transform map  $\eta(x_t^{src}, \vec{c}_{tgt}, t)$  for  $t > 0$  which maps the latent of input  $X^{src}$  to the latent of target  $X^{tgt}$  as a random variable, with following assumption:

$$\eta(x_t^{src}, \vec{c}_{tgt}, t) \sim q(x_t^{tgt} | X^{tgt}). \quad (1)$$

Referring (Salimans and Ho 2022), the loss function  $\mathcal{L}_{DM}$  of diffusion model in  $\mathbf{x}$ -space (sample space) is:

$$\mathcal{L}_{DM} = \mathbb{E}_{(X^{tgt}, \vec{c}_{tgt}), \epsilon, t} \|X^{tgt} - \mathbf{x}_\theta(x_t^{tgt}, \vec{c}_{tgt}, t)\|^2. \quad (2)$$

while the SNR weight is simplified.

Considering the Eq. (1), we rewrite the loss function as

$$\mathcal{L}'_{DM} = \mathbb{E}_{(X^{src}, X^{tgt}, \vec{c}_{tgt}), \epsilon, t} \|X^{tgt} - \mathbf{m}_\theta(x_t^{src}, \vec{c}_{tgt}, t)\|^2 \quad (3)$$

where

$$\mathbf{m}_\theta(x, \vec{c}, t) = \mathbf{x}_\theta(\eta(x, \vec{c}, t), \vec{c}, t). \quad (4)$$

Hence, we predict  $\mathbf{m}_\theta$  by neural network, which is a composition of latent transform function and denoising model.

For the sampling of the reverse process, we exploit the same procedure of the denoising process of diffusion, as

$$x_{t-1}^{tgt} = \tilde{\mu}_t(x_t^{tgt}, \mathbf{m}_\theta(x_t^{tgt}, \vec{c}_{tgt}, t)) + \sigma_t \mathbf{z}, \mathbf{z} \sim N(0, I) \quad (5)$$

where  $\tilde{\mu}_t(x_t, x_0)$  is mean vector of  $q(x_{t-1} | x_t, x_0)$ , introduced in Eq. (7) of (Ho, Jain, and Abbeel 2020).

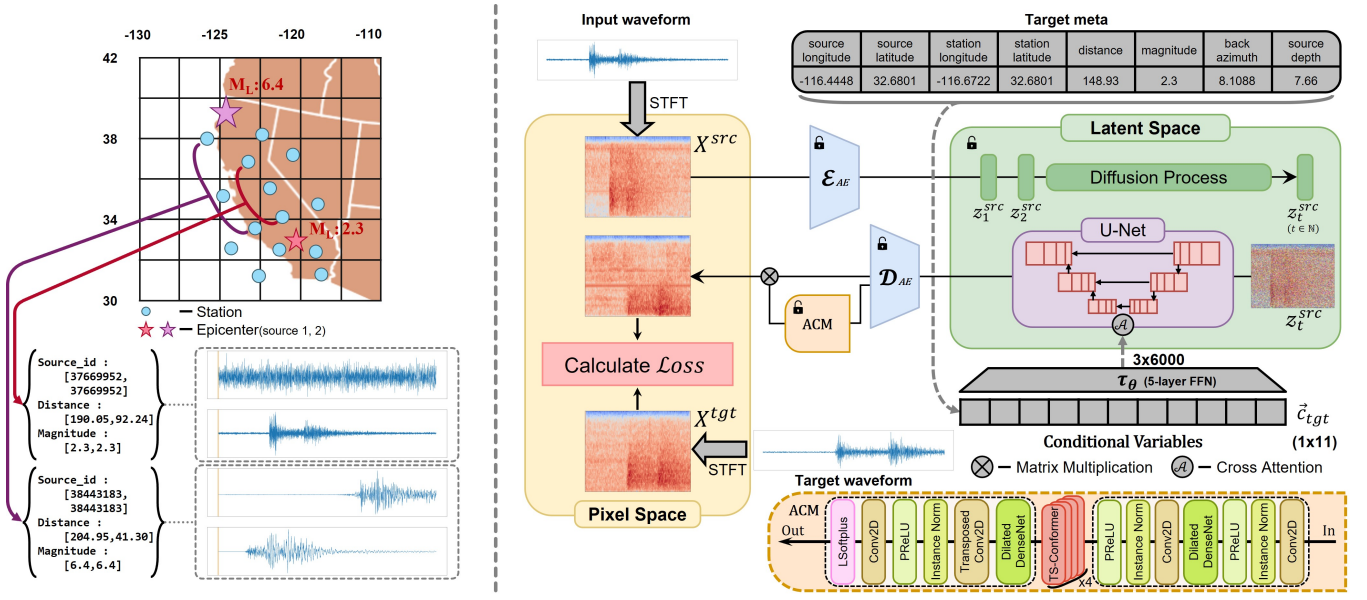


Figure 1: Left : Visualization of SCEDC data using paired waveforms. It shows that earthquake events can be detected at greater distances depending on magnitude. Right : Overall structure of the model.

This is equivalent to conventional denoising process, as

$$\eta(x_t^{tgt}, \vec{c}_{tgt}, t) \stackrel{d}{=} x_t^{tgt} \quad (6)$$

by assumption and thus

$$\mathbf{m}_\theta(x_t^{tgt}, \vec{c}_{tgt}, t) = \mathbf{x}_\theta(x_t^{tgt}, \vec{c}_{tgt}, t). \quad (7)$$

### Latent Diffusion

From the idea of LDM (Rombach et al. 2022), we may consider the autoencoder consist of downsampling module  $\mathcal{E}_{AE}$  and upsampling module  $\mathcal{D}_{AE}$  and construct diffusion model on latent space with smaller dimension. If there is pretrained autoencoder, the LDM loss would be

$$L'_{LDM} = \mathbb{E}_{(Z^{src}, Z^{tgt}, \vec{c}_{tgt}, \epsilon, t)} \|Z^{tgt} - \mathbf{m}_\theta(z_t^{src}, \vec{c}_{tgt}, t)\|^2 \quad (8)$$

where  $Z = \mathcal{E}_{AE}(X)$ ,  $z_t^{src}$  is latent of diffusion process of  $Z^{src}$ .

Since we have no pretrained autoencoder trained on seismic waveforms, we propose the following end-to-end training loss, by further modifying the loss Eq. (8) to train both autoencoder and diffusion model.

$$\mathcal{L}_{ours} = \mathbb{E}_{(X^{src}, X^{tgt}, \vec{c}_{tgt}, \epsilon, t)} \|X^{tgt} - \mathcal{D}_{AE}(\mathbf{m}_\theta(z_t^{src}, \vec{c}_{tgt}, t))\|^2 \quad (9)$$

where  $z_t^{src} = \sqrt{\alpha_t} \mathcal{E}_{AE}(X^{src}) + \sqrt{1 - \alpha_t} \epsilon$ .

### Neural Network Architecture

We utilize the U-Net backbone with cross-attention architecture similar to (Rombach et al. 2022; Ghosal et al. 2023), to represent  $\mathbf{m}_\theta$ , with modification in the domain-specific encoder  $\tau_\theta$  to map  $\vec{c}_{tgt}$  to hidden feature  $\tau_\theta(\vec{c}_{tgt})$ . For the implementation, we construct  $\tau_\theta$  by 5-layer FFN model.

The encoded conditional vector  $\tau_\theta(\vec{c}_{tgt})$  will be provided as a value and key of cross attention module  $Attn(Q, K, V)$  while U-Net feature is provided as query  $Q$ .

For  $\mathcal{E}_{AE}$  and  $\mathcal{D}_{AE}$ , we take same architectures from VAE of (Esser, Rombach, and Ommer 2020) and give a modification on  $\mathcal{D}_{AE}$ . With the vanilla module  $\mathcal{D}_{AE}$ , we find that the proposed model is not effective in accurately predicting the amplitude of the output waveform. Therefore, we propose to attach an additional module ACM after  $\mathcal{D}_{AE}$  to predict the amplitude correction feature and multiply it to the predicted spectrogram. In detail, we utilize the encoder, TSConformer blocks and Magnitude mask decoder module from MP-SeNet (Lu, Ai, and Ling 2023) and provide output of  $\mathcal{D}_{AE}$  and auxiliary phase spectrogram induced by GriffinLim algorithm to correct the amplitude and enhance the quality of generation. Improving the original implementation (Lu, Ai, and Ling 2023) that allows only reducing the output, we add four TSConformer blocks and replace the final sigmoid activation function with Softplus function to provide the ability to increase as well.

### Empirical Verification

The proposed model is trained with a single NVIDIA-RTX A6000 with 48GB memory. We set the number of epochs to 500 and the training batch size to 4. To enhance training efficiency, we apply an accumulation step of 4, resulting in an effective batch size of 16. Training completes in 65 hours, with more implementation details in Appendix C.

### Quantitative Evaluation

To assess the effectiveness of the diffusion model in synthesizing seismic waves, we conducted a comprehensive quantitative analysis focusing on key parameters including P-

EQT	F1-score	Precision	Recall	MAE (s)
P-arrival	0.9728	0.9725	0.9731	0.1116
S-arrival	0.9384	0.9342	0.9428	0.2189

Table 1: Performance of EQT picker on our test dataset. Samples with errors less than 0.5 are considered to be positive.

wave and S-wave arrival times, GMPE analysis, and similarity measures such as envelope correlation, spectrogram image similarity, as well as signal-to-noise ratio (SNR) and peak signal-to-noise ratio (PSNR). In analysis, we generate synthetic waveform  $W^{pred}$  from  $\tilde{c}_{tgt}$  and compare with  $W^{tgt}$  to obtain the qualitative analysis scores.

For comparison, we also trained the following benchmark models: Seismogen (Wang, Trugman, and Lin 2021), Con-seisgen (Li et al. 2024), BBGAN (Florez et al. 2022) and LDM (Rombach et al. 2022). Since the input shape of waveform  $W^{tgt}$  or spectrogram  $X^{tgt}$  is different to each of the models, we give reasonable modifications to them for the training and evaluation. The detailed changelogs are listed in Appendix E.

**Phase Arrival Times** The arrival times of P-wave and S-wave are the most basic, but important properties of seismic waveform, as determining P-wave and S-wave from the seismogram is the first step of earthquake analysis.

Since the synthesized waveform doesn’t have true labels of arrival time, we employed deep-learning based phase picker, EQTransformer (EQT) (Mousavi et al. 2020) with SeisBench (Woollam et al. 2022) implementation. We finetuned the pre-trained EQT model provided by SeisBench. The detailed recipe for EQT training is explained in Appendix D. We present the performance measure of the EQT picker in the test dataset in Table 1. The pick was considered to be true positive when the difference between true label was less than 0.5 seconds.

With such a phase picker, we generated synthetic waveforms for every earthquake in catalog of the test dataset on a random station, determined the phase arrival time of them, and compared them to the ground truth observations.

The results are summarized in the first two columns of Table 2. The resulting phase arrival times of the P wave and the S wave are considered to be close to the ground-truth arrival times, as the MAE values are measured to be small while other benchmark models failed to generate earthquake event signals on correct arrival time. Recall that the phase picker considers the predicted arrival time to be true when it is close to the label with a difference of less than 0.5 seconds.

As can be expected, generation with input waveform  $W^{src}$  gives better results compared to the generation without  $W^{src}$ , i.e. with noise, since missing features of earthquake may gathered from the observation  $W^{src}$ . However, the proposed seismogram synthesis method is considered to be effective in generating waveforms with desired phase arrival times, which is accurate enough to pass the discrimination of phase picker EQT in most cases.

**Similarity Measures** In this section, we compare the synthesized waveform and corresponding spectrogram directly to the observations, with general-purpose similarity measures, the envelope correlation, MSE, SNR and PSNR.

Envelope correlation was calculated to measure the similarity between the envelopes of synthesized and observed seismic waves, providing insights into the overall waveform fidelity. And we apply Savitzky-Golay Filtering (Savitzky and Golay 1964) technique with polyorder 3 before calculate the envelope correlation.

Additionally, we compare the synthesized spectrogram  $X^{syn}$  and spectrogram of observed seismic signals  $X^{tgt}$  to quantify their similarity using image similarity. The comparison of spectrograms would provide evidence of self-consistency of synthesized waveforms since the proposed method aims to synthesize a seismic signal in the frequency domain by generating a spectrogram.

Furthermore, SNR and PSNR metrics were employed to evaluate the quality of the synthesized seismic waves in terms of signal clarity and fidelity to the original data.

These quantitative analyses provide a comprehensive assessment of the performance of the proposed model in accurately reproducing seismic waveforms and will be crucial in validating its applicability in seismic simulations.

The results are summarized in Table 2. The proposed method outperforms the benchmark models on almost all similarity metrics, which may imply that the generated  $X^{syn}$  and  $W^{syn}$  are more realistic in most cases.

**GMPE Analysis** Ground Motion Prediction Equation (GMPE) is a powerful mathematical model used in seismology to predict the ground shaking intensity resulting from earthquakes, and it is crucial for seismic hazard assessment and earthquake engineering. The GMPE model relates earthquake parameters, like local Magnitude  $M_L$  and hypocentral distance  $R_{hyppo}$ , to ground motion characteristics, such as Peak Ground Acceleration (PGA). Since  $M_L$  is obtained from the peak amplitude of the waveforms, the GMPE analysis shows how the scale of the synthesized waveform matches the real observations.

Given the waveform  $W$ , we first compute the local magnitude  $M_L$  using the following formula (equations 1 to 6 of (Uhrhammer et al. 2011))

$$M_L = \log A - \log A_0(R_{hyppo}) \quad (10)$$

where  $A_0(r)$  is attenuation function of southern california peninsula. For detailed computation, we refer the equation 4 to 6 of (Uhrhammer et al. 2011). The station adjustment term was not applied due to a lack of values for recently installed stations.

After determining the local magnitude  $M_L$ , we obtain the PGA value by equation 1 of (Boore et al. 2014), with pynga (Wang 2012) implementation. Since our model doesn’t exploit the focal mechanism information, we set *mech* and *rake* to be 0, which represents unspecified.

Our result of GMPE analysis is depicted in Fig. 2, which reveals that the synthetic seismic waveforms generated by our method closely resemble the observed ground truth in most cases, with similar scale of PGA value. This similarity

Model	Input	Waveform					Spectrogram
		P_MAE (s)	S_MAE (s)	<i>env.corr</i>	SNR	PSNR	MSE
SeismoGen	w/o $W^{src}$	1.9558	3.6246	0.4895	-8.6166	23.5431	1.4124
	w/ $W^{src}$	1.8426	3.3325	0.5454	-8.6282	23.6354	0.8063
ConSeisGen	w/o $W^{src}$	3.9724	6.8992	0.3246	-8.6216	23.6416	0.7461
	w/ $W^{src}$	3.9102	6.8055	0.2980	-8.5341	23.5329	0.9356
BBGAN	w/o $W^{src}$	6.4210	10.416	0.1950	-3.0093	23.7598	1.6150
LDM	w/o $W^{src}$	1.1142	1.7294	0.6932	-3.0202	<b>24.7573</b>	0.2838
	w/ $W^{src}$	0.5633	0.7808	0.7726	-3.0015	19.6269	0.2426
ours	(*)w/o $W^{src}$	0.5025	0.8003	0.7963	-2.9891	24.6816	0.1531
	w/ $W^{src}$	<b>0.4760</b>	<b>0.5476</b>	<b>0.8187</b>	<b>-2.0051</b>	24.6553	<b>0.1512</b>

Table 2: Results of quantitative analysis. Models were evaluated with  $W^{src}$  when it is trained with paired data, otherwise without  $W^{src}$ , except (\*): evaluated without  $W^{src}$ , while the model was trained with paired data.

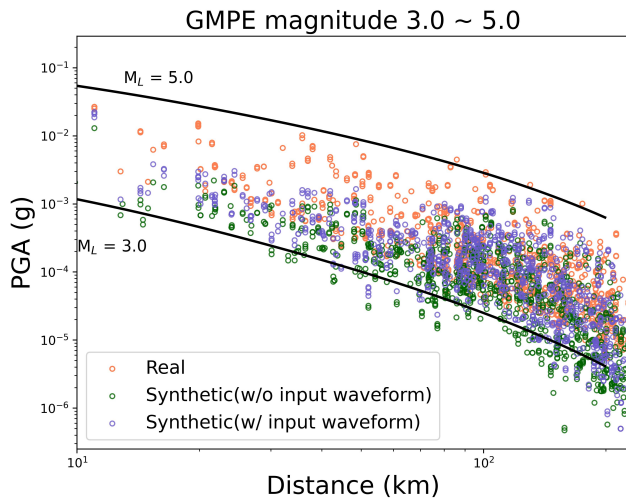


Figure 2: Result of GMPE analysis in PGA values with respect to the distance. The black lines represent the PGA values when  $V_{S30}$  is set to  $760m/s$ , with magnitudes of 3.0 and 5.0, respectively.

also indicates that the magnitude of synthesized waveform is close to the real ones, also in amplitude.

### Qualitative Evaluation

In this section, we present a qualitative analysis of the synthesized seismic waveforms to evaluate the accuracy and reliability of our waveform synthesis methodology.

We generate synthetic waveform on existing station with its location information and compare it against the real waveform. First, we assess the similarity in amplitude and the arrival times of the P and S phases. Next, we evaluate how closely our synthesized spectrograms match the real spectrograms in both the time and frequency domains. Finally, we analyze the frequency content to compare the similarity between synthetic and real waveforms across different magnitudes and to explore the frequency characteristics of

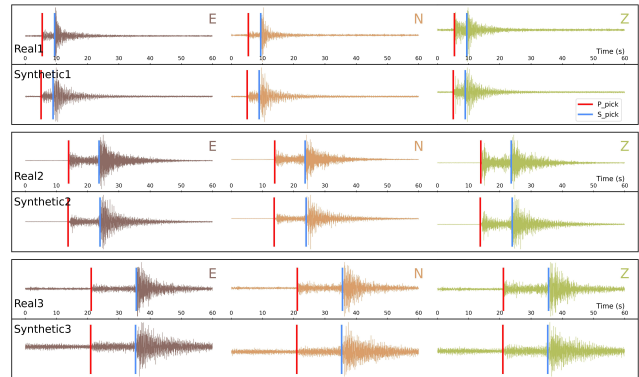


Figure 3: Comparison of 3-component real and synthetic waveform earthquake accelerograms. The top side shows the real waveform and the bottom side shows the synthetic waveform. The arrival times of the P/S phase, detected by EQT, are marked by the red and blue lines.

the energy released for each magnitude.

Additionally, we generate waveforms using both actual and virtual station locations at various distances to investigate how seismic characteristics vary with distance.

**Waveform Analysis** We visually inspect the synthetic waveforms alongside real seismic waveforms to evaluate their similarity in terms of waveform morphology, including the amplitude, shape, and duration of seismic signals.

Fig. 3 shows the synthesized waveform and real waveform respectively. Notably, both synthesized waveform and real waveform depict similar patterns of seismic activity, including distinct seismic phases and their corresponding arrivals. This alignment underscores the effectiveness of our synthesis approach in accurately replicating the seismic signal's morphology and temporal evolution. More waveform examples can be found in Appendix G.

**Spectrogram Comparison** We also show the output spectrogram of proposed model, compared to the real spectro-

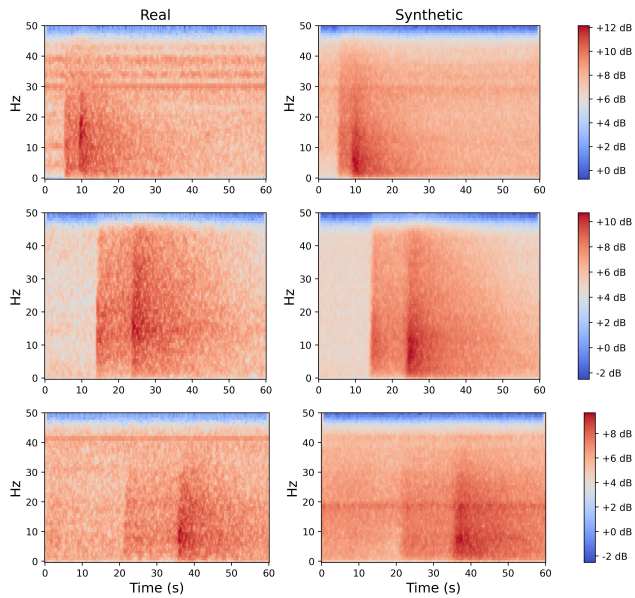


Figure 4: Comparison of real and synthetic spectrograms.

gram to examine their time-frequency characteristics, providing insights into the distribution of energy across different frequency bands over time.

In Fig. 4 we show the comparison of spectrograms, where each corresponds to the waveforms in Fig. 3. Upon comparing the synthesized spectrogram with the real spectrogram, several key observations come to light. Both spectrograms exhibit remarkable similarities in terms of phase arrival times and frequency band distribution, indicative of the efficacy of our synthesis approach in capturing essential seismic signal characteristics. However, it is discernible that the synthesized spectrogram exhibits a slightly lower resolution compared to the real spectrogram, with some details appearing less defined. This reduction in resolution is particularly evident in the depiction of fine-scale frequency variations and subtle signal features. Despite this difference, the overall agreement between the synthesized and real spectrograms underscores the fidelity of our synthesis method in reproducing the fundamental characteristics of seismic signals. More spectrogram examples are shown in Appendix G.

**Frequency Content Analysis** In this section, we analyze how the energy released during an earthquake using frequencies. This analysis is closely related to the concept of corner frequency (Boore 1983) and the seismic moment ( $M_0$ ). The corner frequency is generally associated with the earthquake’s magnitude. Specifically, the corner frequency identifies the point at which high-frequency energy begins to decline sharply, indicating that larger earthquakes generally have lower corner frequencies. The  $M_0$  represents the total energy released by the earthquake, which corresponds to an increase in amplitude on the spectrum as the earthquake’s magnitude increases. By comparing synthetic and observed seismic signals, we aim to evaluate the similarity between the two characteristics of corner frequency and

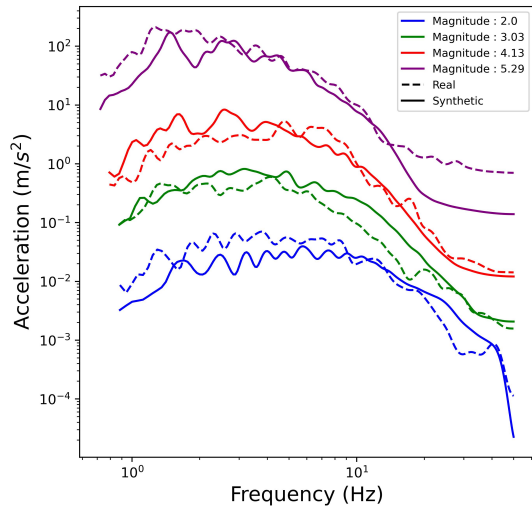


Figure 5: Frequency contents of synthetic waveform compared to the real waveform.

$M_0$  across different magnitudes. We apply both Fast Fourier Transform (FFT) and Konno-Ohmachi-smoothing (Konno and Ohmachi 1998) technique to enhance our comparison. Also, we apply Wood-Anderson simulations (Havskov and Ottemöller 2010) to compare results from distinct stations.

The resulting spectra are shown in Fig. 5. We observe significant differences in corner frequency and  $M_0$  across different earthquake magnitudes, that the corner frequency reduces and  $M_0$  increases when the magnitude grows.

**Waveform Analysis on Synthetic Stations** By arranging virtual observation stations in a linear manner, spatial variations of seismic waves could be observed, facilitating an understanding of seismic event characteristics. The synthesized seismic waves reflected seismic activity at the virtual observation stations, enabling exploration of subsurface structures and seismic wave propagation characteristics.

The sections in Fig. 6 represented the positions of observation stations horizontally and represented the temporal and frequency characteristics of seismic activity vertically. Through such visualization, comparisons between synthesized and observed seismic waves could be conducted, assessing the fidelity of the synthesized seismic waves in reflecting seismic events. Results from section plots clearly visualized spatial and temporal variations of seismic activity, serving as crucial criteria for evaluating the extent to which our synthesis method accurately reproduces actual observed results. More section plot examples of seismic events are provided in Appendix H.

## Ablation Studies

Compared to the conventional latent diffusion model, we introduced two major components, the efficient learning framework and amplitude correction module, to generate high-quality seismic waveforms. In this section, we present the results of the ablation study to evaluate the role of each component.



seismic domain-specific metrics, such as envelope correlation and P/S phase arrival times, for expert-level comparison.

## References

2007. *Appendix C: Coordinate Transformations*, 456–501. John Wiley & Sons, Ltd. ISBN 9780470099728.
- An, Y.; Guo, J.; Ye, Q.; Childs, C.; Walsh, J.; and Dong, R. 2021. Deep convolutional neural network for automatic fault recognition from 3D seismic datasets. *Computers & Geosciences*, 153: 104776.
- Beyreuther, M.; Barsch, R.; Krischer, L.; Megies, T.; Behr, Y.; and Wassermann, J. 2010. ObsPy: A Python toolbox for seismology. *Seismological Research Letters*, 81(3): 530–533.
- Boore, D. M. 1983. Stochastic simulation of high-frequency ground motions based on seismological models of the radiated spectra. *Bulletin of the Seismological Society of America*, 73(6A): 1865–1894.
- Boore, D. M.; Stewart, J. P.; Seyhan, E.; and Atkinson, G. M. 2014. NGA-West2 equations for predicting PGA, PGV, and 5% damped PSA for shallow crustal earthquakes. *Earthquake Spectra*, 30(3): 1057–1085.
- Chen, G.; Li, J.; and Guo, H. 2024. Deep Generative Model Conditioned by Phase Picks for Synthesizing Labeled Seismic Waveforms With Limited Data. *IEEE Transactions on Geoscience and Remote Sensing*, 62: 1–15.
- Esser, P.; Rombach, R.; and Ommer, B. 2020. Taming Transformers for High-Resolution Image Synthesis. arXiv:2012.09841.
- Florez, M. A.; Caporale, M.; Buabthong, P.; Ross, Z. E.; Asimaki, D.; and Meier, M. 2022. Data-Driven Synthesis of Broadband Earthquake Ground Motions Using Artificial Intelligence. *Bulletin of the Seismological Society of America*, 112(4): 1979–1996.
- Ghosal, D.; Majumder, N.; Mehrish, A.; and Poria, S. 2023. Text-to-Audio Generation using Instruction Guided Latent Diffusion Model. In *Proceedings of the 31st ACM International Conference on Multimedia*, 3590–3598.
- Havskov, J.; and Ottemöller, L. 2010. *Magnitude*, 151–191. Dordrecht: Springer Netherlands. ISBN 978-90-481-8697-6.
- Ho, J.; Jain, A.; and Abbeel, P. 2020. Denoising diffusion probabilistic models. *Advances in neural information processing systems*, 33: 6840–6851.
- Isola, P.; Zhu, J.-Y.; Zhou, T.; and Efros, A. A. 2017. Image-To-Image Translation With Conditional Adversarial Networks. In *Proceedings of the IEEE Conference on Computer Vision and Pattern Recognition (CVPR)*.
- Katsanos, E. I.; Sextos, A. G.; and Manolis, G. D. 2010. Selection of earthquake ground motion records: A state-of-the-art review from a structural engineering perspective. *Soil dynamics and earthquake engineering*, 30(4): 157–169.
- Konno, K.; and Ohmachi, T. 1998. Ground-motion characteristics estimated from spectral ratio between horizontal and vertical components of microtremor. *Bulletin of the Seismological Society of America*, 88(1): 228–241.
- Li, Y.; Yoon, D.; Ku, B.; and Ko, H. 2024. ConSeis-Gen: Controllable Synthetic Seismic Waveform Generation. *IEEE Geoscience and Remote Sensing Letters*, 21: 1–5.
- Lu, Y.-X.; Ai, Y.; and Ling, Z.-H. 2023. Mp-senet: A speech enhancement model with parallel denoising of magnitude and phase spectra. *arXiv preprint arXiv:2305.13686*.
- McPhillips, D. F.; Herrick, J. A.; Ahdi, S.; Yong, A. K.; and Haefner, S. 2020. Updated Compilation of VS30 Data for the United States. Accessed on Month Day, Year.
- Mousavi, S. M.; and Beroza, G. C. 2022. Deep-learning seismology. *Science*, 377(6607): eabm4470.
- Mousavi, S. M.; Ellsworth, W. L.; Zhu, W.; Chuang, L. Y.; and Beroza, G. C. 2020. Earthquake transformer—an attentive deep-learning model for simultaneous earthquake detection and phase picking. *Nature communications*, 11(1): 3952.
- Rombach, R.; Blattmann, A.; Lorenz, D.; Esser, P.; and Ommer, B. 2022. High-resolution image synthesis with latent diffusion models. In *Proceedings of the IEEE/CVF conference on computer vision and pattern recognition*, 10684–10695.
- Saad, O. M.; Chen, Y.; Siervo, D.; Zhang, F.; Savvaidis, A.; Huang, G.-c. D.; Igonin, N.; Fomel, S.; and Chen, Y. 2023. EQCCT: A production-ready earthquake detection and phase picking method using the compact convolutional transformer. *IEEE Transactions on Geoscience and Remote Sensing*.
- Salimans, T.; and Ho, J. 2022. Progressive Distillation for Fast Sampling of Diffusion Models. In *International Conference on Learning Representations*.
- Savitzky, A.; and Golay, M. J. 1964. Smoothing and differentiation of data by simplified least squares procedures. *Analytical chemistry*, 36(8): 1627–1639.
- SCEDC. 2013. Southern California Earthquake Center.
- Shi, Y.; Lavrentiadis, G.; Asimaki, D.; Ross, Z. E.; and Azizadenesheli, K. 2024. Broadband Ground-Motion Synthesis via Generative Adversarial Neural Operators: Development and Validation. *Bulletin of the Seismological Society of America*, 114(4): 2151–2171.
- Sohl-Dickstein, J.; Weiss, E.; Maheswaranathan, N.; and Ganguli, S. 2015. Deep unsupervised learning using nonequilibrium thermodynamics. In *International conference on machine learning*, 2256–2265. PMLR.
- Uhrhammer, R. A.; Hellweg, M.; Hutton, K.; Lombard, P.; Walters, A. W.; Hauksson, E.; and Oppenheimer, D. 2011. California Integrated Seismic Network (CISN) Local Magnitude Determination in California and Vicinity. *Bulletin of the Seismological Society of America*, 101(6): 2685–2693.
- Wang, F. 2012. pynga. <https://github.com/fengw/pynga>.
- Wang, T.; Trugman, D.; and Lin, Y. 2021. SeismoGen: Seismic waveform synthesis using GAN with application to seismic data augmentation. *Journal of Geophysical Research: Solid Earth*, 126(4): e2020JB020077.
- Woollam, J.; Münchmeyer, J.; Tilmann, F.; Rietbrock, A.; Lange, D.; Bornstein, T.; Diehl, T.; Giunchi, C.; Haslinger, F.; Jozinović, D.; Michelini, A.; Saul, J.; and Soto, H. 2022.



SeisBench—A Toolbox for Machine Learning in Seismology. *Seismological Research Letters*, 93(3): 1695–1709.

Zhu, W.; Mousavi, S. M.; and Beroza, G. C. 2019. Seismic Signal Denoising and Decomposition Using Deep Neural Networks. *IEEE Transactions on Geoscience and Remote Sensing*, 57(11): 9476–9488.

## A Pre-processing Recipe

### A.1 Conditional Vector Pre-processing

We explain the process of  $\vec{c}_{tgt}$  construction. Recall the variables that we are used to synthesize waveform are:

1.  $s_{lat}, s_{lon}$  : latitude and longitude of the station to observe the waveform data.
2.  $e_{lat}, e_{lon}$  : latitude and longitude of epicenter.
3.  $e_{dep}$  : depth of the hypocenter, unit of kilometers.
4.  $e_m$  : magnitude of the earthquake.

We preprocessed those variables to construct an 11-dimensional condition vector and later provide it to our condition encoder module  $\tau_\theta$ .

First of all, we encode locational information  $s_{lat}, s_{lon}, e_{lat}$  and  $e_{lon}$  with the following process:

1. Normalize the values to get  $s'_{lat}, s'_{lon}, e'_{lat}$  and  $e'_{lon}$  with following:

$$s'_{lat} = \frac{s_{lat} - l_{lat}}{u_{lat} - l_{lat}}, e'_{lat} = \frac{e_{lat} - l_{lat}}{u_{lat} - l_{lat}}, s'_{lon} = \frac{s_{lon} - l_{lon}}{u_{lon} - l_{lon}} \text{ and } e'_{lon} = \frac{e_{lon} - l_{lon}}{u_{lon} - l_{lon}} \quad (11)$$

where  $(l_{lat}, u_{lat})$  and  $(l_{lon}, u_{lon})$  represent the lower and upper bounds of latitude and longitude, respectively, for the region of interest. In our dataset, which was collected from the SCEDC API, the region of interest is Southern California, with

$$(l_{lat}, u_{lat}) = (32.024809, 36.151200) \text{ and } (l_{lon}, u_{lon}) = (-120.444000, -115.222300) \quad (12)$$

2. Motivated from polar coordinate transformation(Coo 2007), which is commonly used in GPS field, we further encode normalized coordinate to following:

$$\begin{aligned} c_{sta} &= (\cos(s'_{lat})\cos(s'_{lon}), \sin(s'_{lat})\cos(s'_{lon}), \sin(s'_{lon})) \\ c_{epi} &= (\cos(e'_{lat})\cos(e'_{lon}), \sin(e'_{lat})\cos(e'_{lon}), \sin(e'_{lon})) \end{aligned} \quad (13)$$

Secondly, we compute the back azimuth angle  $Azi$  and encode by

$$c_{azi} = (\cos(Azi), \sin(Azi)) \quad (14)$$

Lastly, we compute and normalized epicentral distance  $R_{epi}$ , focus depth  $d_s$  and magnitude  $M_L$ . Each are normalized by following formula:

$$\begin{aligned} R'_{epi} &= (R_{epi} - 125.542401)/55.810322 \\ d'_s &= (d_s - 8.564146)/4.658161 \\ M'_L &= (M_L - 2.0)/6.4 \end{aligned} \quad (15)$$

Concatenating the processed features  $c_{sta}, c_{epi}, c_{azi}, R'_{epi}, d'_s$  and  $M'_L$ , we get an 11-dimensional conditional vector  $\vec{c}_{tgt}$  for our problem, the synthesis of seismic ground motion.

### A.2 spectrogram construction

The generation target of our model is spectrogram, which is in time-frequency domain. We report the process of spectrogram construction as pre-processing. We employed the STFT (Short-Time Fourier Transform) with a hop length 16. Given that the spectrogram's scale is closely related to the earthquake's amplitude, we used an  $nfft$  and  $window\ length$  of 128 and applied a logarithmic scale transformation for better scale adjustment. Consequently, the original waveform data of size  $3 \times 6000$  was reshaped into  $3 \times 64 \times 376$ .

## B Dataset Construction

We used the SCEDC (SCEDC 2013) dataset provided by SeisBench (Woollam et al. 2022). From this dataset, we selected waveforms with a sampling rate of 100Hz that included 60 seconds from the earthquake and applied a bandpass filter in the 1 ~ 45Hz range to construct our data. However, each source initially had fewer than 13 stations on average. To address this, we utilized the obspy API (Beyreuther et al. 2010) to save waveforms. By using `source_id` from SCEDC during the years 2016 to 2019, we constructed a new dataset with approximately 30 stations per source. The station list in (Uhrhammer et al. 2011) was used to calculate the local magnitude. The final dataset used for training averaged 34 stations per source. The Table 4 shows the count of datasets we used.

The  $V_{S30}$  information was sourced from (McPhillips et al. 2020) and used only during the GMPE analysis, not during the training or model inference processes. The average value was used if multiple  $V_{S30}$  values were present for a single station code. For station codes without  $V_{S30}$  data,  $760m/s$  was assigned to negate the influence of  $V_{S30}$  during GMPE analysis.

Features	Train	Test
#observations	71488	17878
#source event	2098	525
#station	149	149
#station per events	34.07	34.05
average magnitude	2.45	2.45
average epicentral distance	125.25	126.71
average focus depth	8.51	8.65

Table 4: Features of the constructed SCEDC dataset

## C Implementation details

We implement the proposed model with following implementation details.

During the training,  $W_{src}$  is fixed for a specific earthquake source ID, and  $W_{tgt}$  is sampled from earthquakes with the same source ID. Among these, if metadata contained P/S phase labels, samples are randomly selected from those with labels. If P/S phase labels are absent, samples are chosen randomly without considering P/S phase labels. And also we conduct preprocessing of seismic data.

We implement using single NVIDIA-RTX A6000 with 48GB memory. For training, we set the number of epochs to 500 and the training batch size to 4. To enhance training efficiency, we apply an accumulation step 4, resulting in an effective batch size of 16. For the loss, we set the maximum diffusion steps to  $T = 1000$  and SNR weight 5. We minimize the loss by AdamW optimizer with learning rate  $10^{-5}$  and *pytorch.optim* defaults. During the training, we applied learning rate decaying technique with linear scheduler. The total duration of training is approximately 65 hours.

## D EQT Training Details

We used EQTransformer (Mousavi et al. 2020) provided by SeisBench (Woollam et al. 2022). Starting from pre-trained model provided by SeisBench, we finetune the model with our dataset, with the same training protocol. After standardizing the waveforms, we trained the model using the Adam optimizer, with a batch size of 512 and a learning rate of  $10^{-3}$ , for 100 epochs. Other hyperparameters of the optimizer were set to default. For hyperparameter search, the learning rate ranged from  $10^{-2}$  to  $10^{-5}$ , and the performance was best when it was  $10^{-3}$ .

## E Details on Benchmark Models

### E.1 SeismoGen (Wang, Trugman, and Lin 2021)

SeismoGen is a CGAN-based model that generates waveforms conditioned on the presence of seismic events (e.g., P or S waves). The Discriminator takes both the waveform and the presence of seismic events as inputs. It then divides the waveform into high and low frequency components, analyzing each to determine if waveform is real or synthetic. SeismoGen used data from three stations in Oklahoma: V34A, V35A, and V36A, while we used data from 149 stations from SCEDC. Our synthesis approach used station and earthquake information instead of presence of seismic events. SeismoGen generated waveforms as 40 seconds at 40Hz, but we aimed for 60 seconds at 100Hz. We used an input noise length of 1500 and added upsampling at the end of the first convolution layer. The basic training used noise as input, and for comparison with our model, we also trained using waveform. When using waveforms, we modified each pipeline to utilize one ENZ channel. The hyper-parameters we used included the Generator learning rate and Discriminator learning rate are set to  $10^{-4}$  and  $10^{-6}$ , using the RMSprop optimizer over 3000 epochs. The  $\lambda$  is set to 10 when using noise and 15 when using the input waveform. We saved the best model based on envelope correlation. We experimented with learning rates ranging from  $10^{-4}$  to  $10^{-7}$ , using both Adam and RMSprop optimizers. The value of  $\lambda$  was tested at 5, 10, and 15. The best-performing combination of these parameters was selected for the final model. Additionally, the results reported in Table 2 reflect the best performance achieved across 30 iterations. Addressing the instability of the original method, we added the L1 loss Eq. (16) from pix2pix (Isola et al. 2017) as an additional loss term to improve training stability.

### E.2 ConSeisGen (Li et al. 2024)

ConSeisGen is an ACGAN-based model that generates waveforms conditioned on the epicentral distance. The Discriminator consists of two components:  $D_P$ , which learn determining whether the waveform is real or synthetic, and  $D_Q$ , which learn regression estimating the distance between the epicenter and the station. While ConSeisGen generated waveforms with 3 channels and a length of 4096, we aimed to generate waveforms with 3 channels and a length of 6000. We modified the first linear layer and removed upsampling in the final layer. ConSeisGen used KiK-net data, which began recording shortly before the arrival of the P-wave. However, the SCEDC data utilized in this model was recorded from the onset of the earthquake for a duration of 60 seconds. ConSeisGen generates waveforms based on the epicentral distance. However, waveforms can vary even at the same

distance due to factors like magnitude and geological conditions. To generate waveforms for specific locations, we utilized minimal additional condition such as station data and source data along with the epicentral distance. The hyper-parameters we used included the Generator learning rate and Discriminator learning rate are set to  $2 \times 10^{-4}$  and  $10^{-5}$ , using the Adam optimizer over 5000 epochs. Referring eq.4 of (Li et al. 2024), the loss function consists of Adversarial Loss, Regression Loss ( $L_{reg}$ ), and Diversity Improvement Loss ( $L_{di}$ ). The  $L_{reg}$  computes the  $l1$  loss between  $D_Q$ 's output and the condition vector, with the  $\lambda_{reg}$  set to 1. The  $L_{di}$  aims to prevent mode collapse by maximizing the distance between feature maps, with  $\lambda_{di}$  set to 10 when using noise and 5 when using waveforms. We experimented with learning rates ranging from  $10^{-4}$  to  $10^{-6}$ , using both Adam and RMSprop optimizers. The value of  $\lambda_{di}$  was tested at 5, 10, and 15, while  $\lambda_{reg}$  was fixed at 1. The best-performing combination of these parameters was selected for the final model. Additionally, the results reported in Table 2 reflect the best performance achieved across 30 iterations. Addressing the instability of the original method, we added the L1 loss Eq. (16) from pix2pix(Isola et al. 2017) as an additional loss term to improve training stability.

$$L_{L1}(G) = \mathbb{E}_{x,y,z} [\|x_{tgt} - G(z, y)\|_1] \quad (16)$$

### E.3 BBGAN (Florez et al. 2022)

BBGAN is a conditional generative model within the Wasserstein GAN framework. The original conditions of BBGAN are  $V_{S30}$ , earthquake magnitude, and epicentral distance. We modified conditional vector to ours, add conditional vector encoder  $\tau_\theta$  to both generator and discriminator, modified the last upsample layer of generator to have scale factor 3 (original: 2), and lastly increased the number of hidden features of last convolution block of discriminator, corresponding to our waveform shape (3, 6000). Those changes allows the model to generate (3, 6000) shape waveform from the provided conditional vector. To further improve the performance, we replaced all relu activations of generator and leaky relu activations of discriminator to gelu activation. Additionally, while the original BBGAN paper utilized data from Japanese networks K-NET and KiK-net with earthquake magnitudes larger than 4.5, our approach employed data from the SCEDC (SCEDC 2013) with earthquake magnitude larger than 2.0 for training. In the training process, we set 500 training epoch and batch size 32, and Adam optimizer with learning rate  $5 \times 10^{-7}$  and  $\beta = (0.9, 0.999)$ . Also the final loss function is composed of adversarial loss, L1 reconstruction loss, and a KL divergence term. The L1 regularization term was set to 25, and the KL regularization term was set to 0.01. For evaluation during the validation loop, envelope correlation was used as the performance metric. During the training, the linear learning rate decay technique was applied.

### E.4 LDM (Rombach et al. 2022)

**VAE (Esser, Rombach, and Ommer 2020) pretraining** Due to lack of pretrained weights of VAE trained on seismic spectrogram, we first need to train VAE to encode  $X^{tgt}$  and  $X^{src}$  to latent vector  $Z^{tgt}$  and  $Z^{src}$ .

Employing equation (25) of (Rombach et al. 2022), we set the loss function for VAE training is:

$$L_{total} = \min_{\mathcal{E}_{AE}, \mathcal{D}_{AE}} \max_{\psi} [L_{rec}(x, \mathcal{D}_{AE}(\psi(x))) - L_{adv}(\mathcal{D}_{AE}(\mathcal{E}_{AE}(x))) + \log D_\psi(x) + \lambda_{kl} KL] \quad (17)$$

where  $\lambda_{kl}$  is low weighted Kullback-Libler regularization term by factor  $10^{-6}$ .

Unfortunately, the VAE training on our spectrogram diverged, due to difficulty on magnitude processing. Therefore, we apply standardization on spectrogram to relax the problem. And the latent space size is  $64 \times 16 \times 94$ .

We report reconstruction performance of the Auto-encoder model using the proposed our metrics. The reconstruction performance results as follow in Table 5.

Table 5: Reconstruction result

Model	waveform				spectrogram	
	P_MAE (s)	S_MAE (s)	envelope corr	SNR	PSNR	MSE
VAE	0.5155	0.7066	0.7567	-2.9984	25.1800	0.2459

**LDM (Rombach et al. 2022)** We train LDM using the pretrained VAE Appendix E.4 and DDPM(Ho, Jain, and Abbeel 2020) scheduler. Additionally, the overall model architecture is adapted and modified base on the TANGO (Ghosal et al. 2023) model and code. But, while TANGO models incorporate text-encoded conditions through Large Language Model, the seismic data does not exist text conditions. Therefore, we employ our preprocessed conditions and apply our conditional vector encoder  $\tau_\theta$  for training. During model training, the learning target is set the samples from the DDPM scheduler. Training is conduct using two methods and training losses.

- Eq. (18): not utilizing the characteristic of paired data
- Eq. (19): utilizing the characteristic of paired data

We set the hyperparameters for the AdamW optimizer as follows: an initial learning rate  $10^{-5}$  and  $\beta = (0.9, 0.999)$ , and a weight decay of  $10^{-2}$  and adam epsilon  $10^{-8}$ . Also, we apply learning rate decaying technique with linear scheduler. The training batch size is set 4 with accumulation step of 4, resulting in a total effective batch size of 16. The model is trained for 500 epochs. The results indicate that training with paired data outperforms training without paired data.

$$L'_{LDM} = \mathbb{E}_{(Z^{tgt}, \vec{c}_{tgt}), \epsilon, t} \|Z^{tgt} - \mathbf{x}_{\theta}(z_t^{tgt}, \vec{c}_{tgt}, t)\| \quad (18)$$

$$L'_{LDM} = \mathbb{E}_{(Z^{src}, Z^{tgt}, \vec{c}_{tgt}), \epsilon, t} \|Z^{tgt} - \mathbf{m}_{\theta}(z_t^{src}, \vec{c}_{tgt}, t)\| \quad (19)$$

## F Qualitative Analysis on Ablation Models

This section is dedicated to the qualitative analysis of the models mentioned in Table 3. The figure compares the Real observation (Real), our model, end-to-end train (w/o ACM), and LDM + paired data. The human-labeled P/S arrival times of the earthquake are indicated by orange and black lines, while the P/S arrival times detected by EQT for each waveform are shown in red and blue.

### F.1 Positive samples

We first list the positive samples, which are the results that all models generated realistic waveforms with accurate phase arrivals.

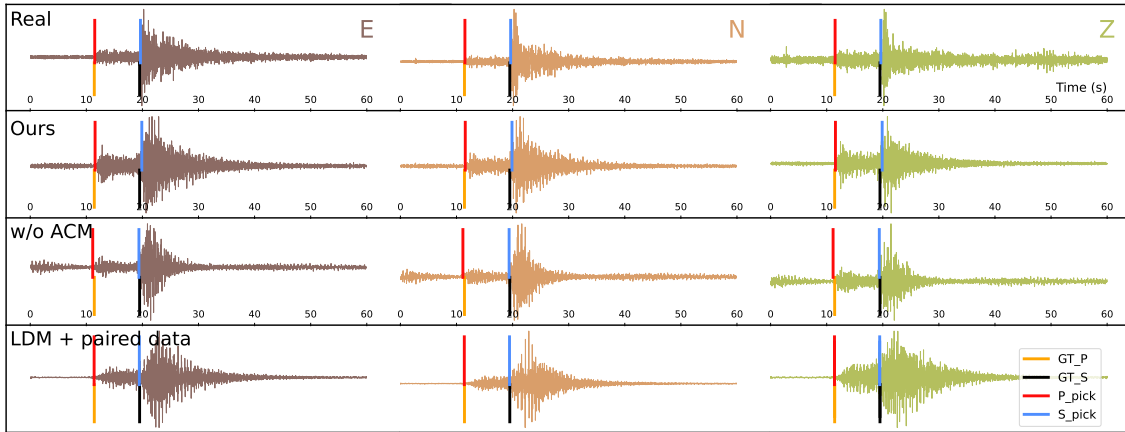


Figure 7: Positive synthesis results of our model and ablation models, compared to the real observation.

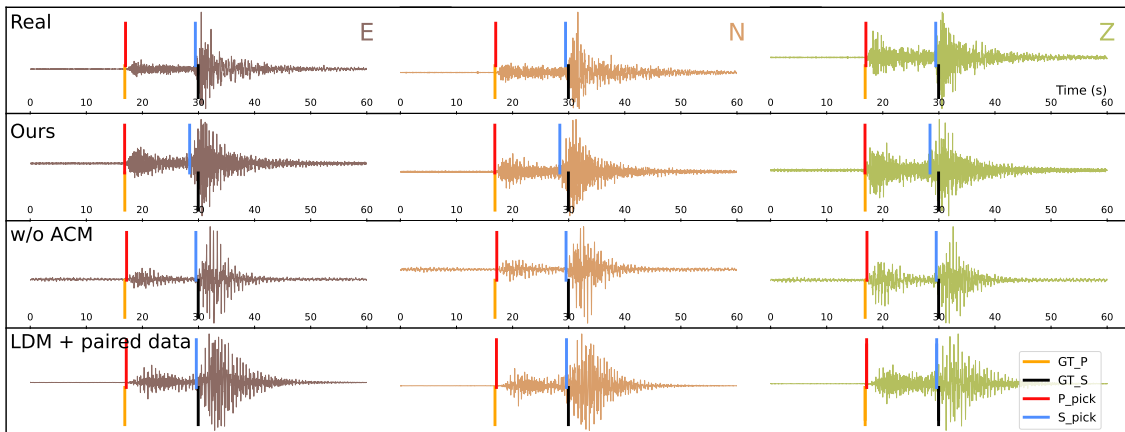


Figure 8: Positive synthesis results of our model and ablation models, compared to the real observation.

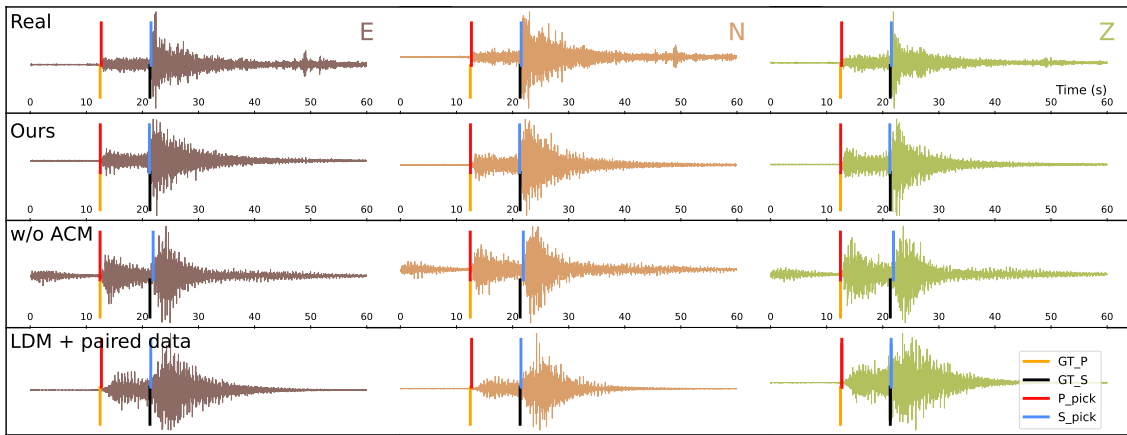


Figure 9: Positive synthesis results of our model and ablation models, compared to the real observation.

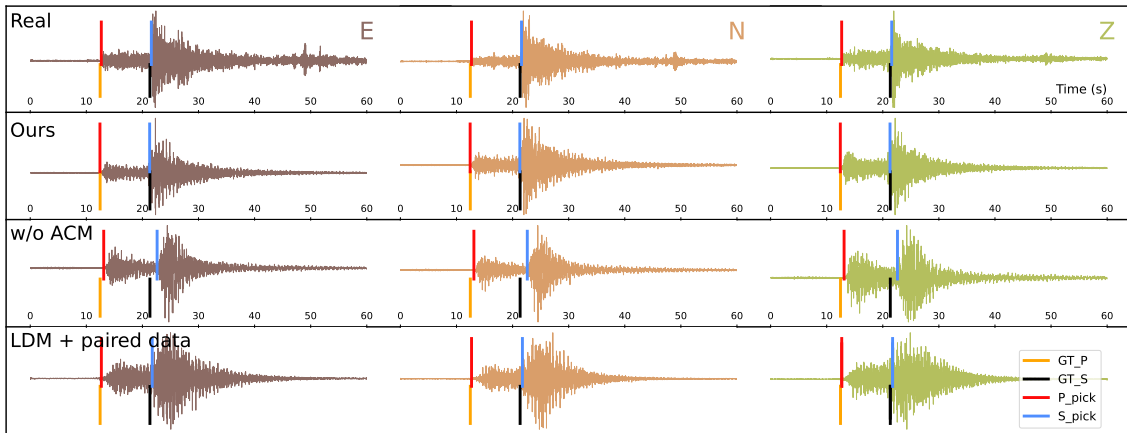


Figure 10: Positive synthesis results of our model and ablation models, compared to the real observation.

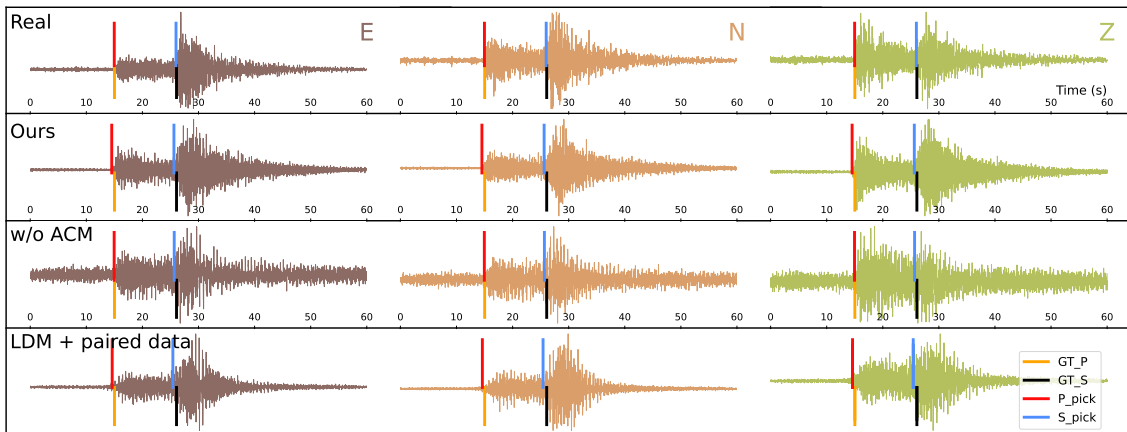


Figure 11: Positive synthesis results of our model and ablation models, compared to the real observation.

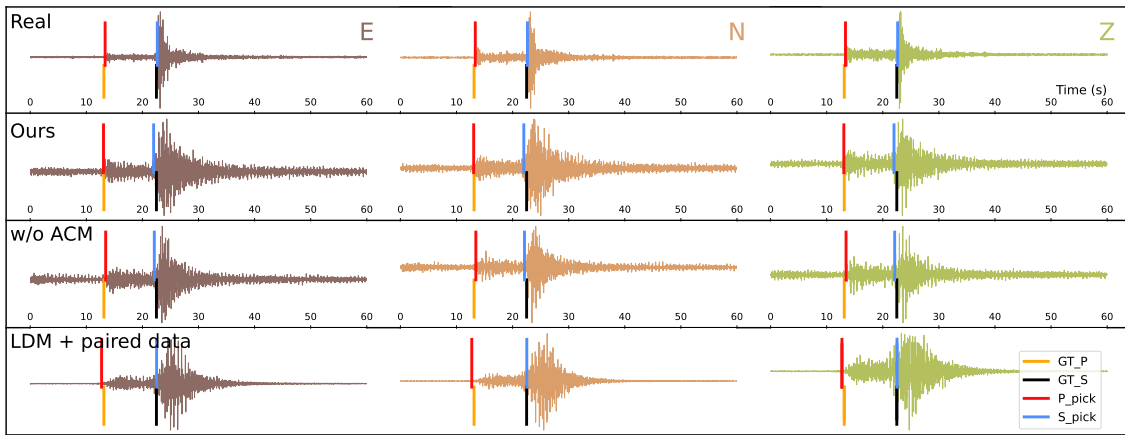


Figure 12: Positive synthesis results of our model and ablation models, compared to the real observation.

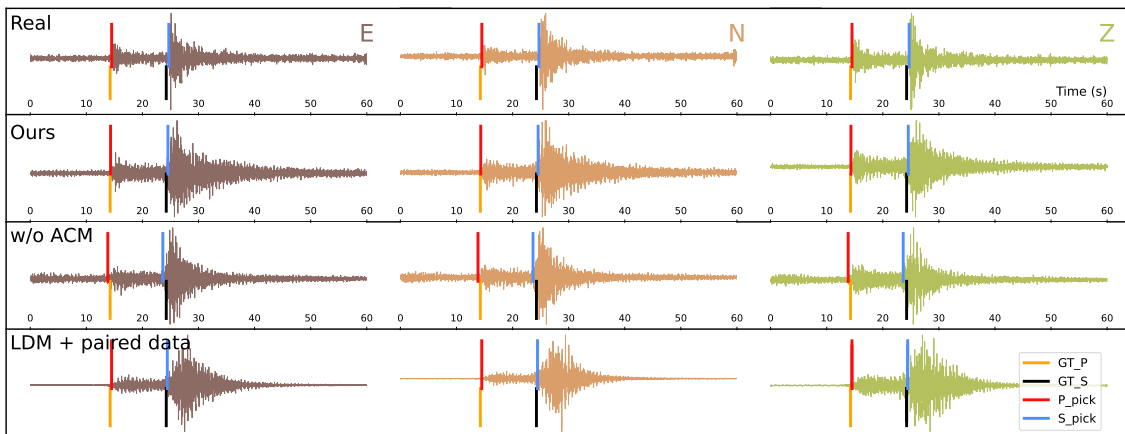


Figure 13: Positive synthesis results of our model and ablation models, compared to the real observation.

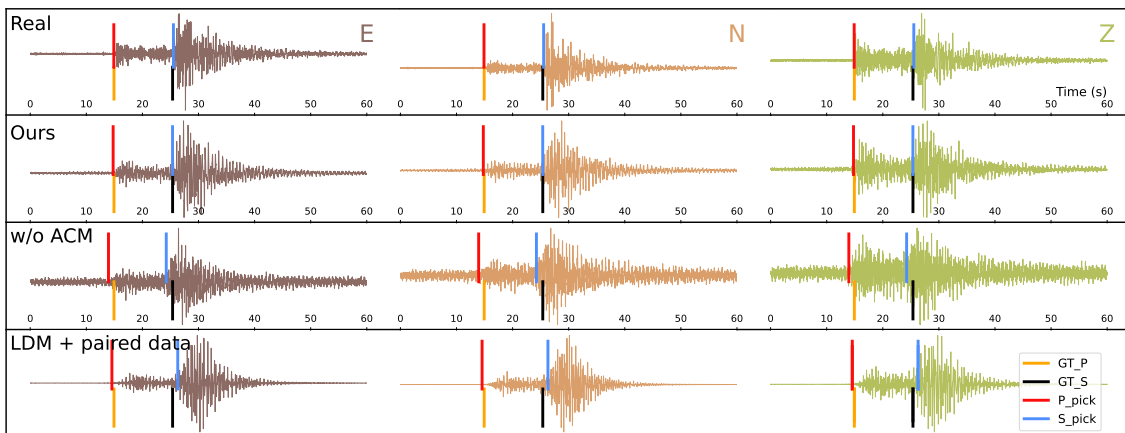


Figure 14: Positive synthesis results of our model and ablation models, compared to the real observation.

## F.2 Negative Samples

We also include the results of the synthesis that at least one of the models failed to generate realistic and accurate waveforms.

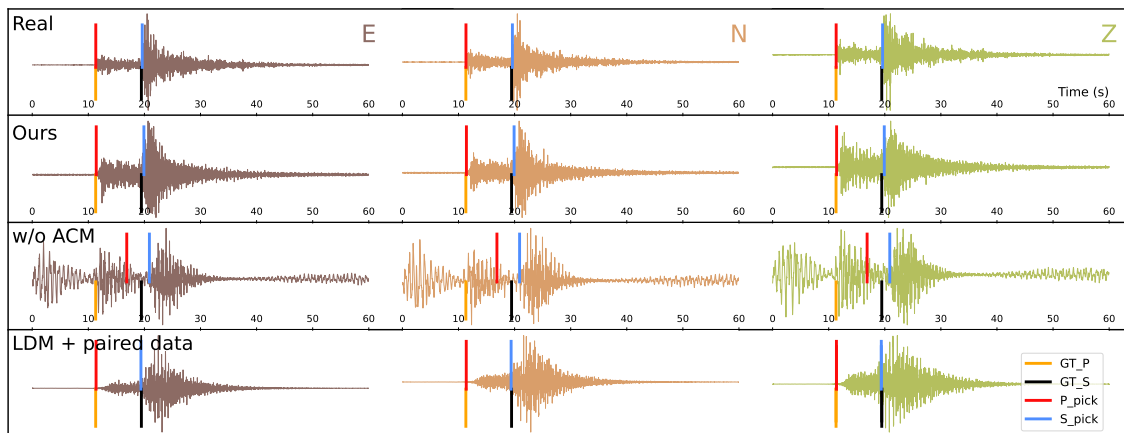


Figure 15: Negative synthesis results of our model and ablation models, compared to the real observation.

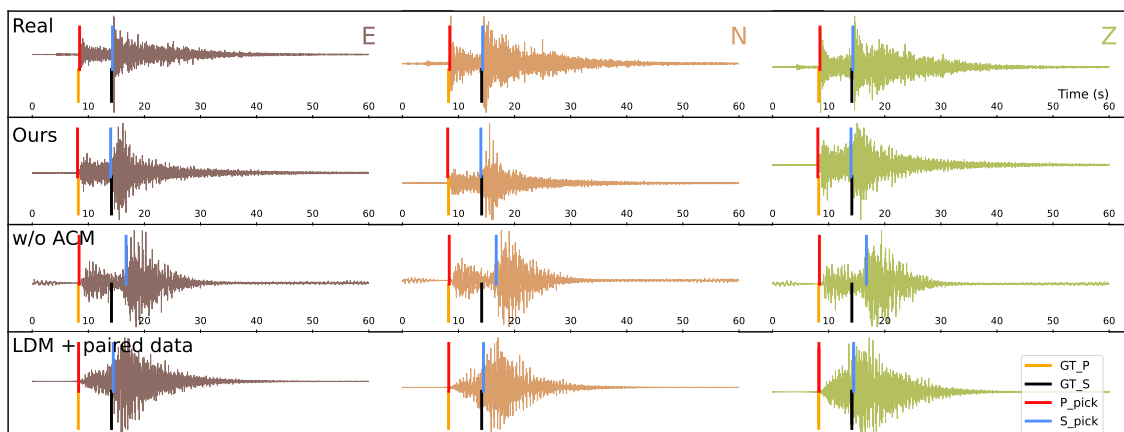


Figure 16: Negative synthesis results of our model and ablation models, compared to the real observation.

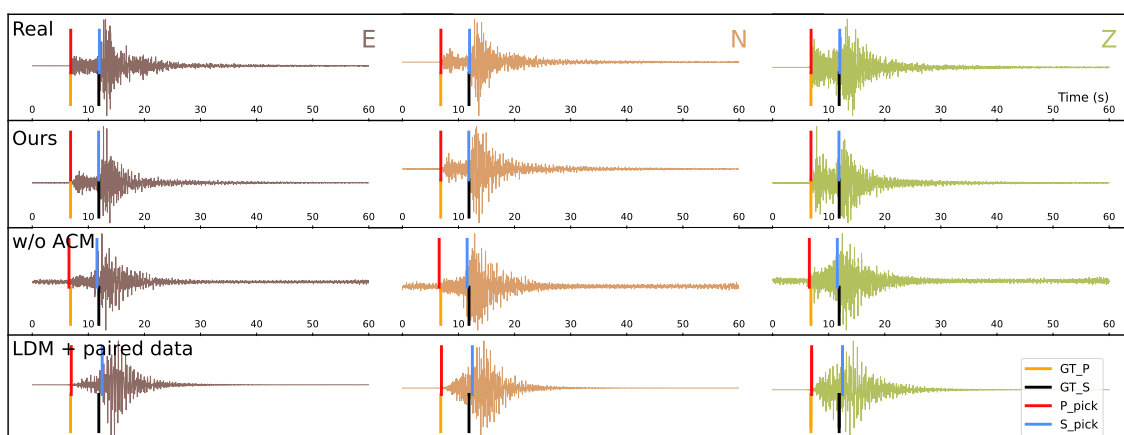


Figure 17: Negative synthesis results of our model and ablation models, compared to the real observation.



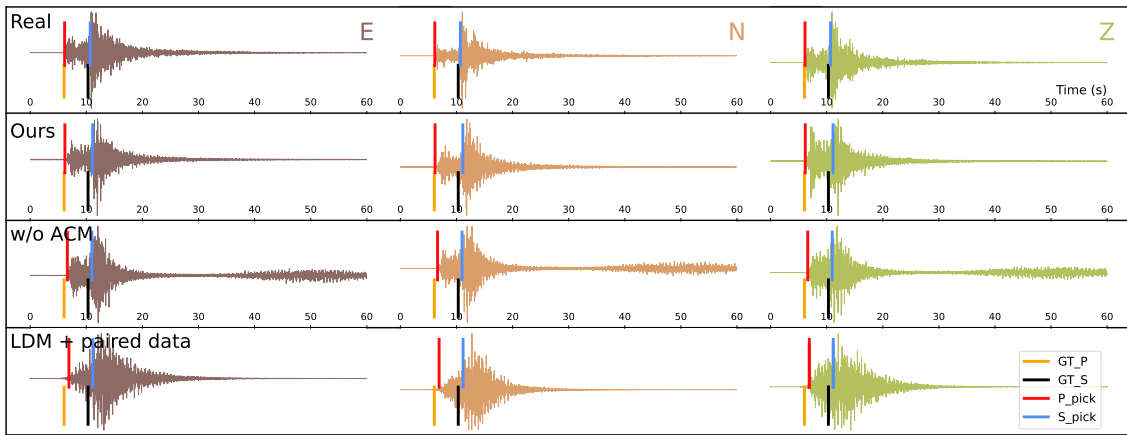


Figure 18: Negative synthesis results of our model and ablation models, compared to the real observation.

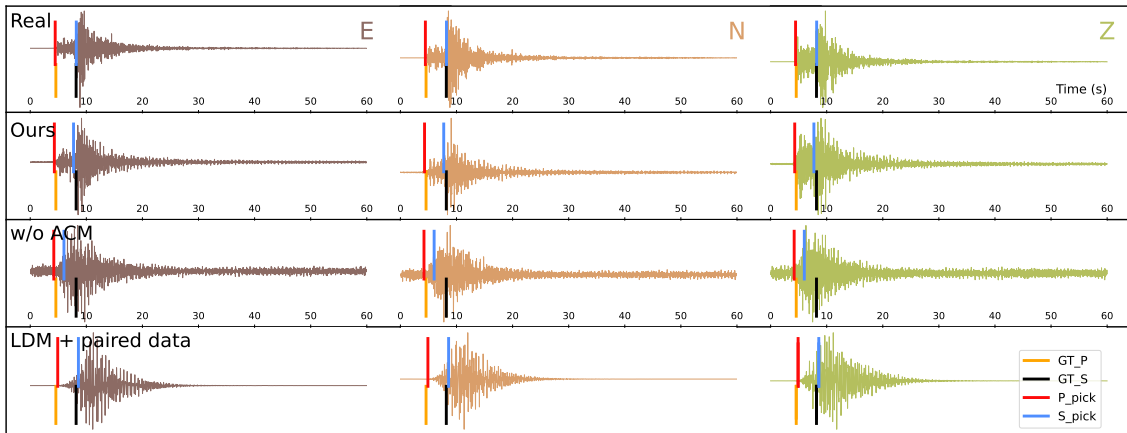


Figure 19: Negative synthesis results of our model and ablation models, compared to the real observation.

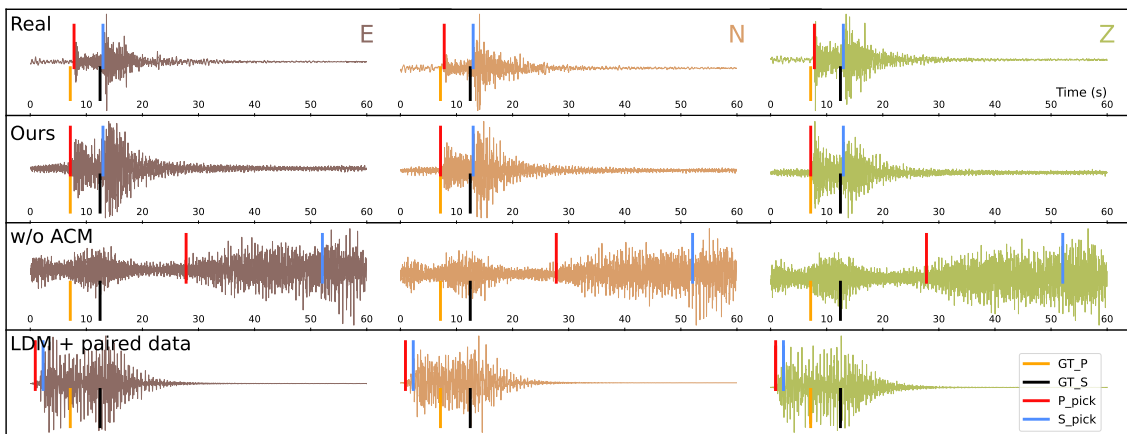


Figure 20: Negative synthesis results of our model and ablation models, compared to the real observation.

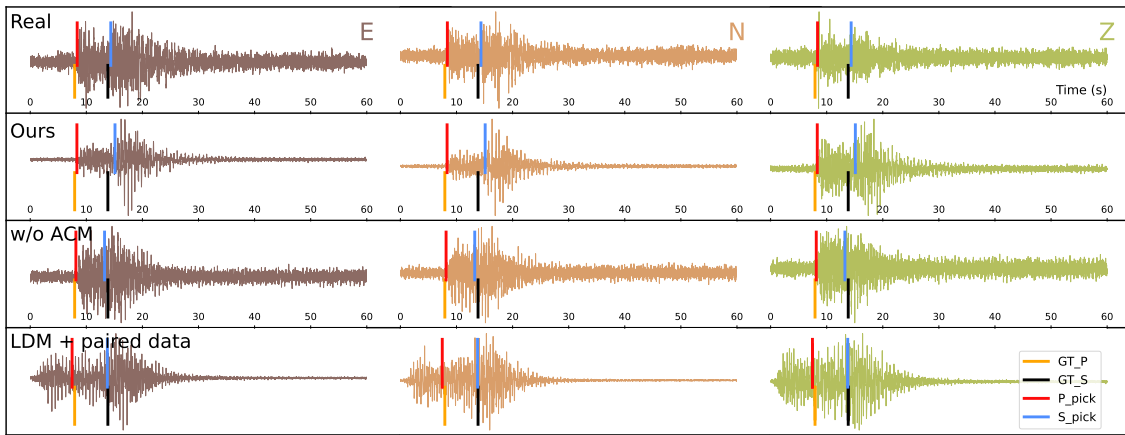


Figure 21: Negative synthesis results of our model and ablation models, compared to the real observation.

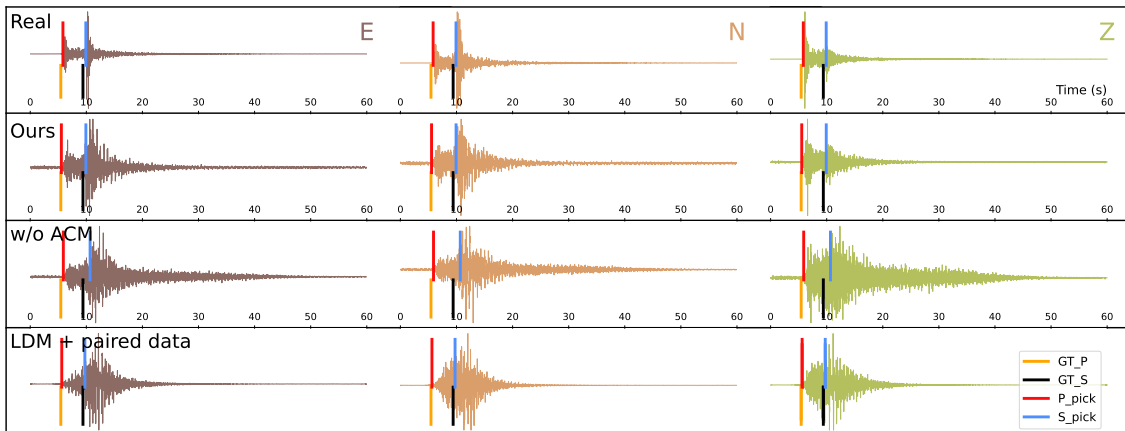
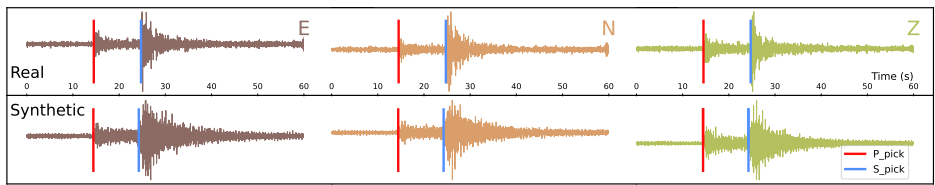


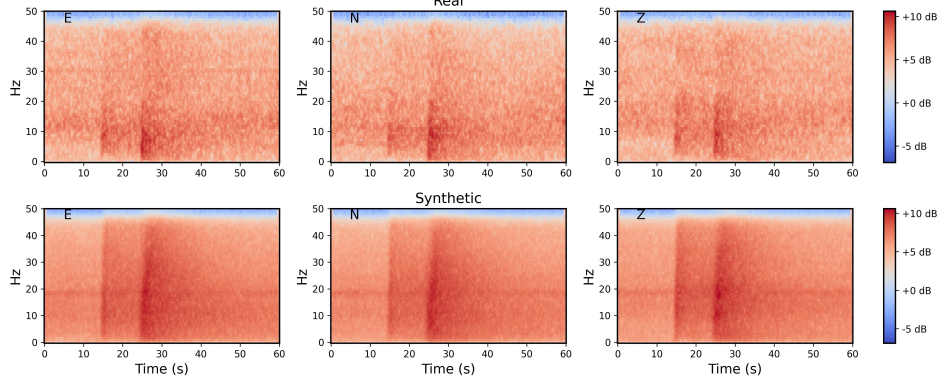
Figure 22: Negative synthesis results of our model and ablation models, compared to the real observation.

## G Additional Figures: Waveform and Spectrogram

This section presents the waveforms and spectrograms shown in Fig. 3 and Fig. 4. The seismic data we used consist of 3-components, ENZ. Each pair displays the same waveform and spectrogram, with the top representing the real observation and the bottom representing the synthetic generated by our model. The red and blue lines on the waveforms indicate the P/S arrival times.

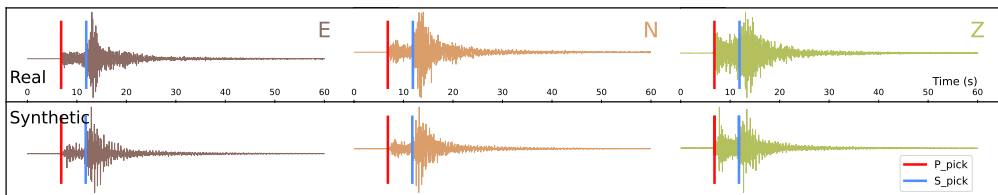


(a) waveforms

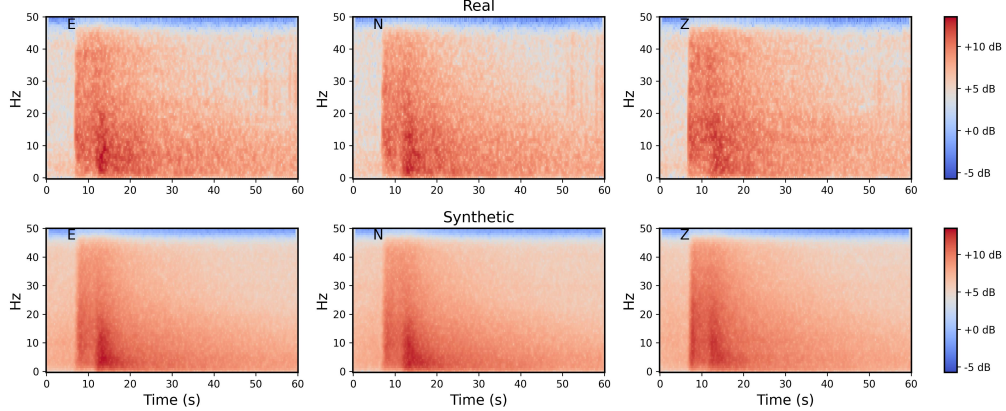


(b) spectrograms

Figure 23: Synthesis results of our model compared to the real observation.

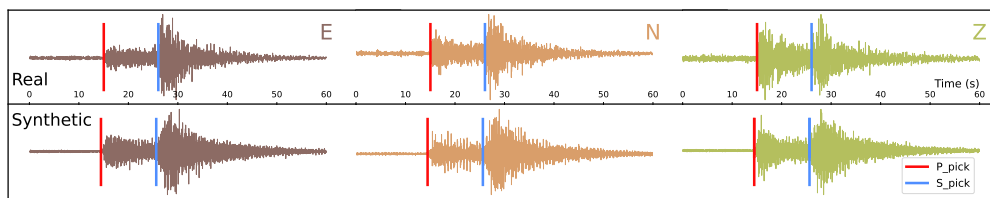


(a) waveform

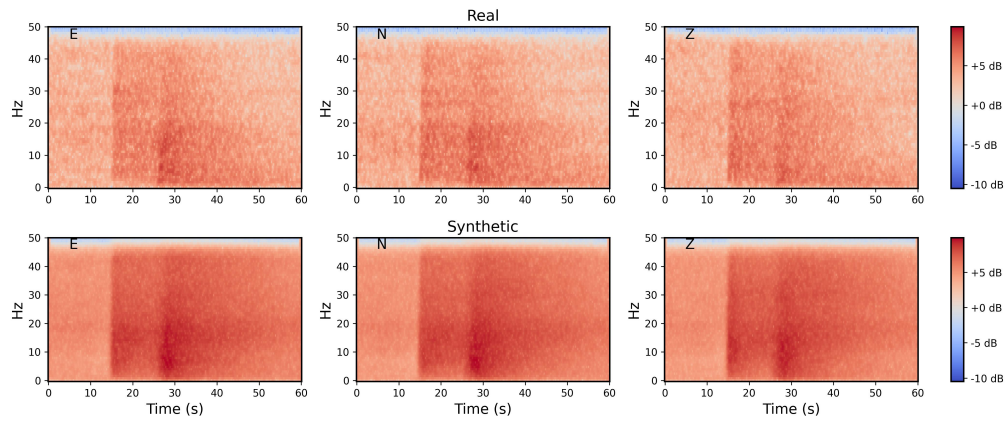


(b) spectrogram

Figure 24: Synthesis results of our model compared to the real observation.

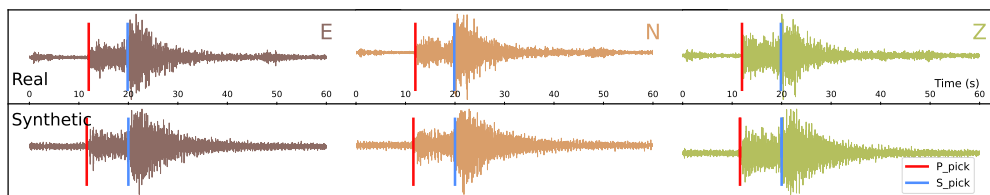


(a) waveform

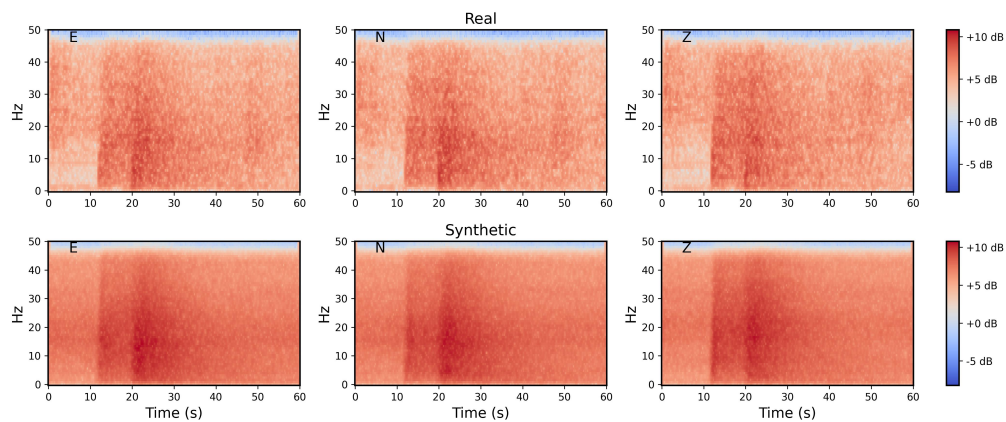


(b) spectrogram

Figure 25: Synthesis results of our model compared to the real observation.

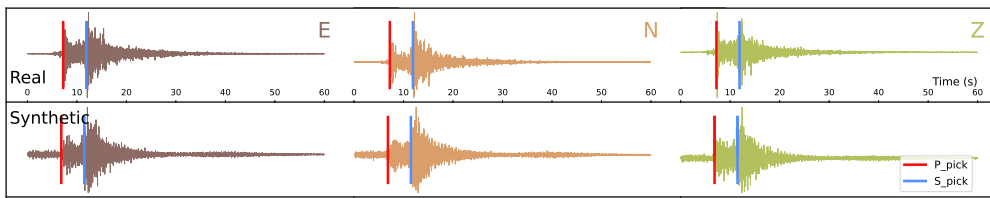


(a) waveform

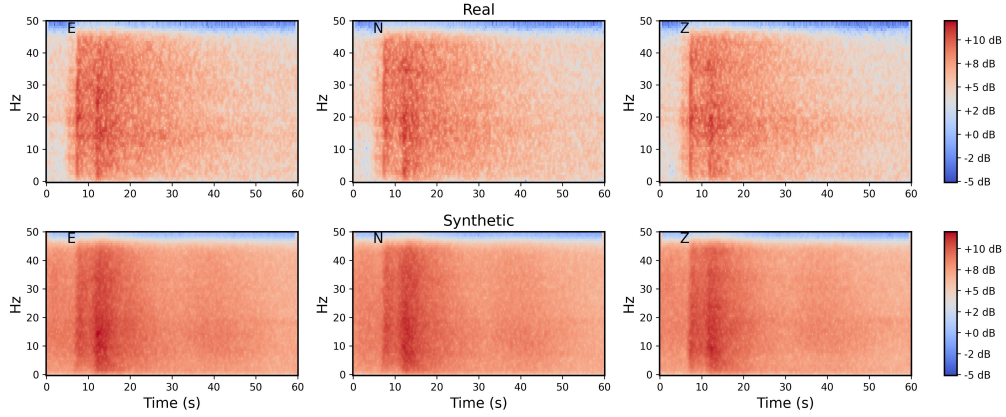


(b) spectrogram

Figure 26: Synthesis results of our model compared to the real observation.

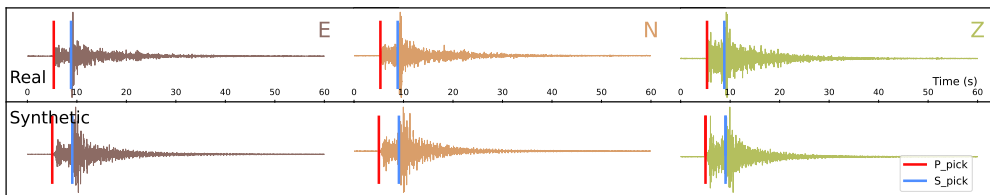


(a) waveform

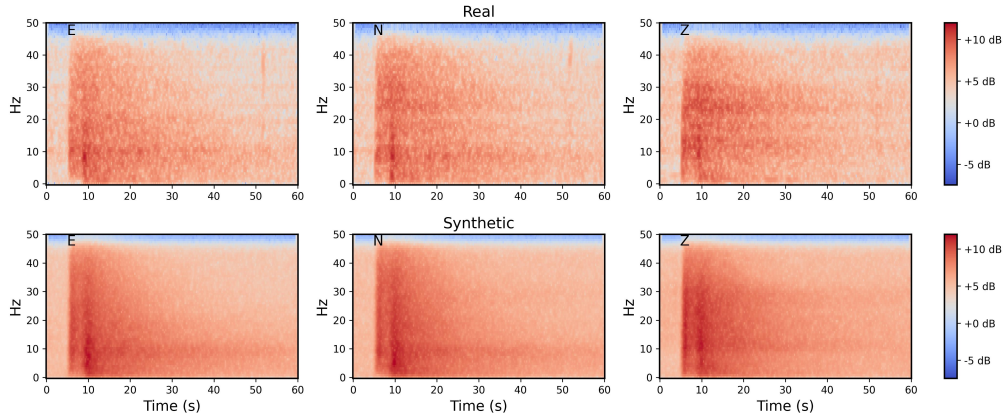


(b) spectrogram

Figure 27: Synthesis results of our model compared to the real observation.

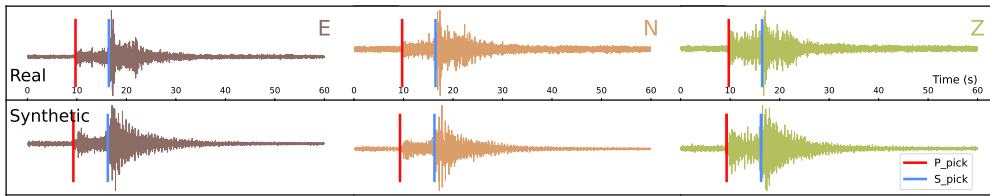


(a) waveform

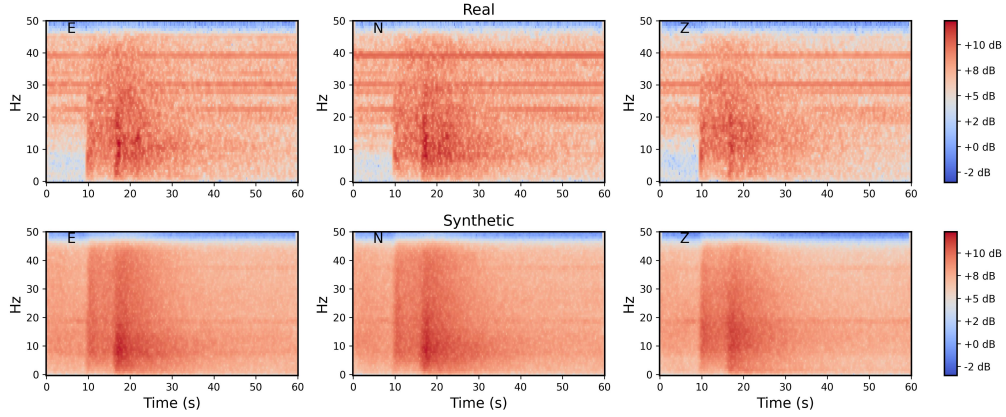


(b) spectrogram

Figure 28: Synthesis results of our model compared to the real observation.

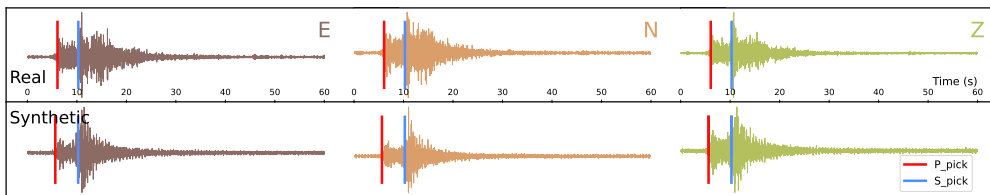


(a) waveform

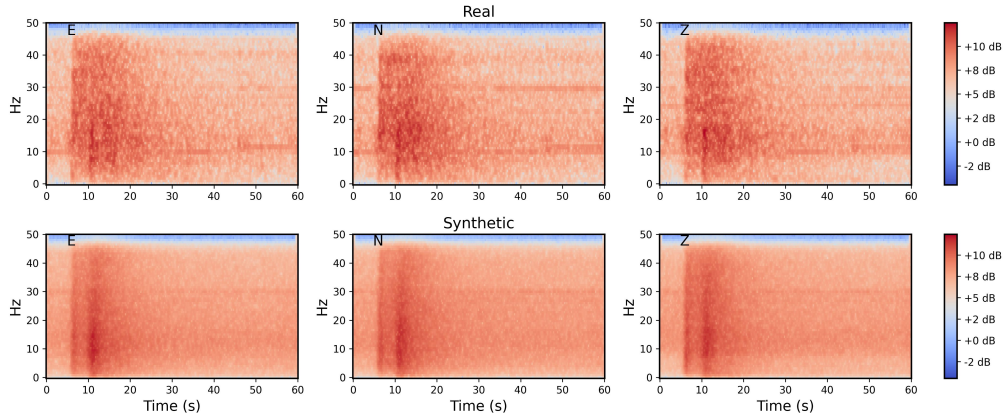


(b) spectrogram

Figure 29: Synthesis results of our model compared to the real observation.

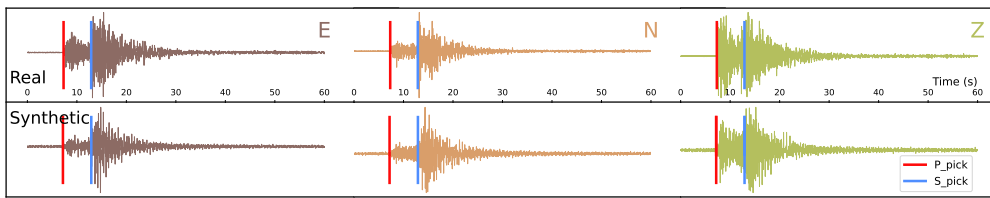


(a) waveform

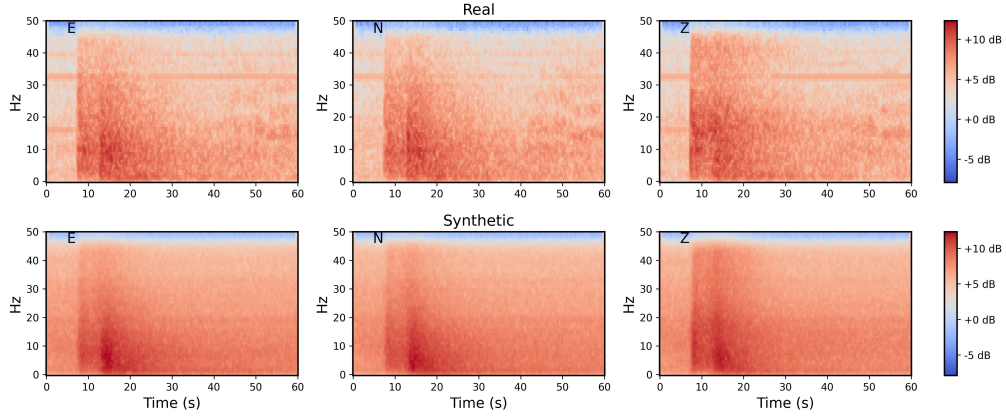


(b) spectrogram

Figure 30: Synthesis results of our model compared to the real observation.

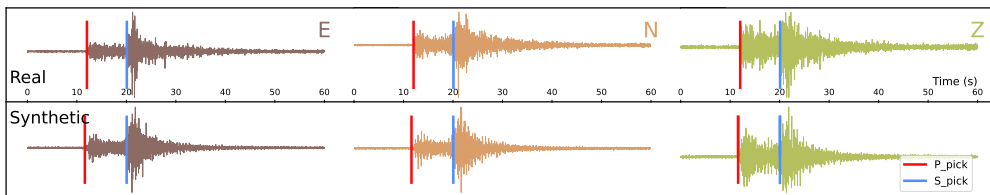


(a) waveform

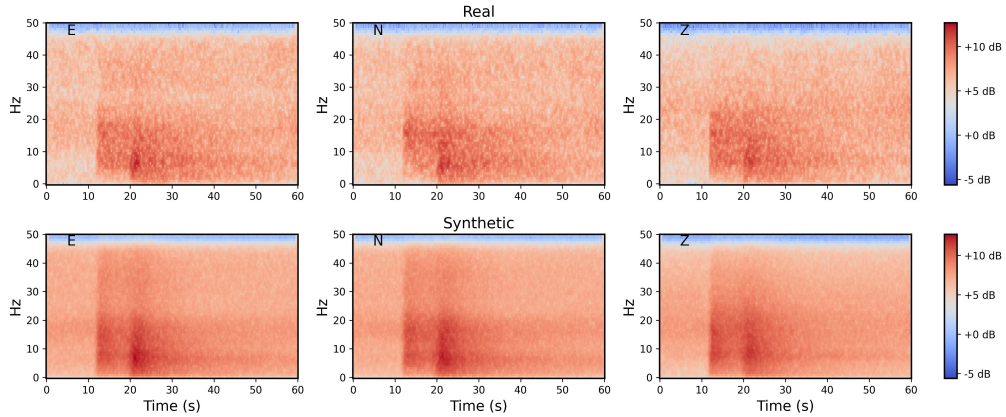


(b) spectrogram

Figure 31: Synthesis results of our model compared to the real observation.

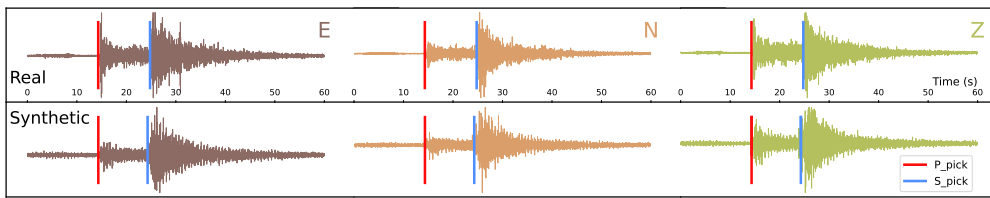


(a) waveform

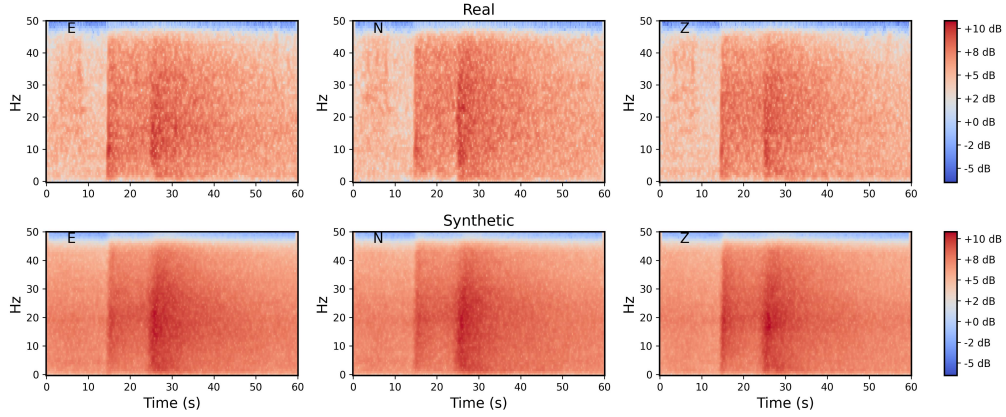


(b) spectrogram

Figure 32: Synthesis results of our model compared to the real observation.

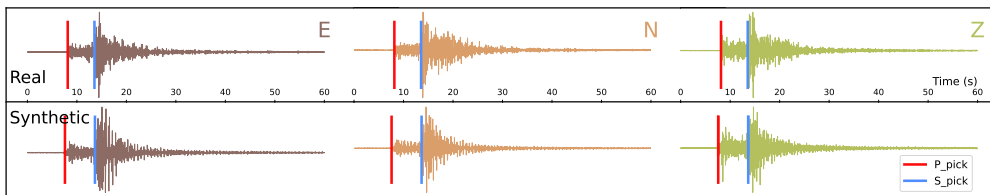


(a) waveform

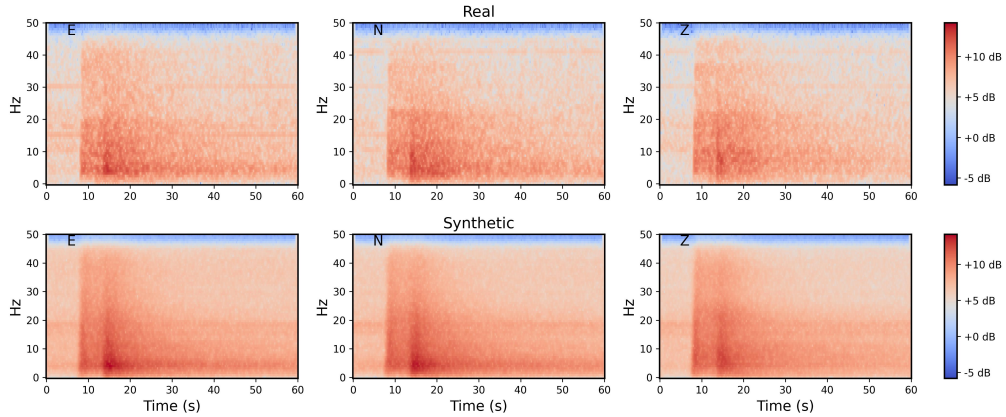


(b) spectrogram

Figure 33: Synthesis results of our model compared to the real observation.



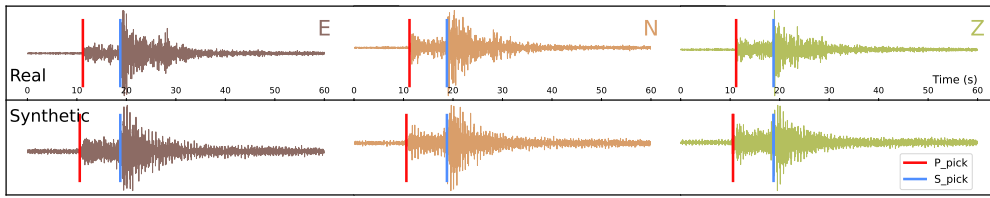
(a) waveform



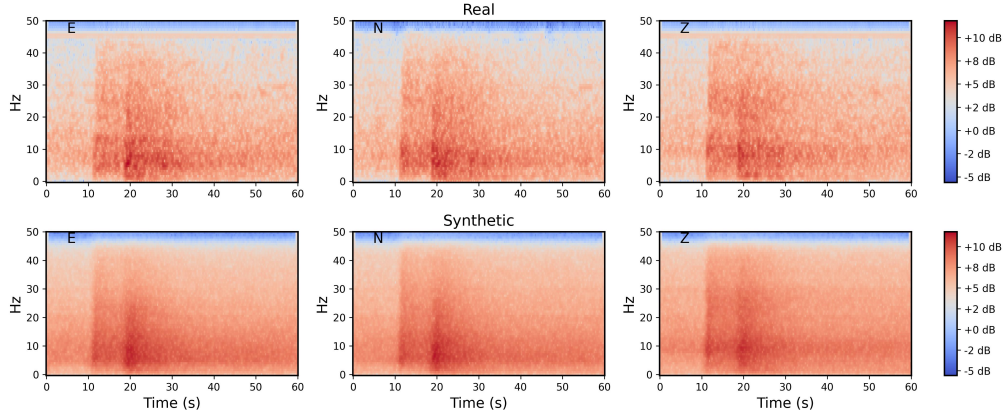
(b) spectrogram

Figure 34: Synthesis results of our model compared to the real observation.





(a) waveform

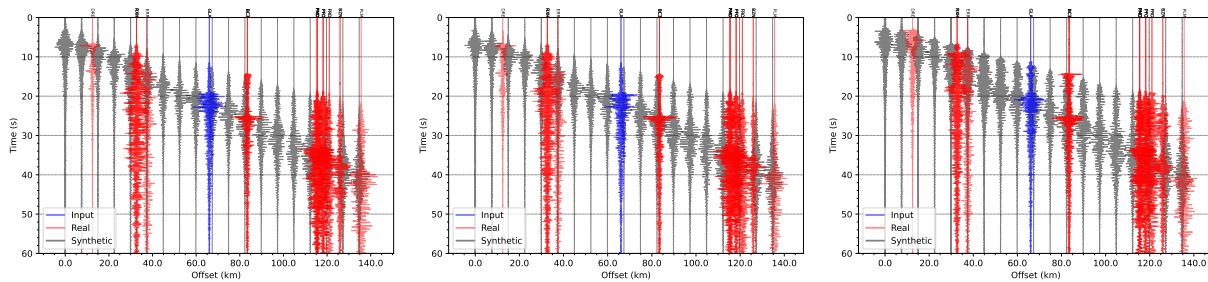


(b) spectrogram

Figure 35: Synthesis results of our model compared to the real observation.

## H Additional figures: Section plot

The section plot is constructed by following process. Initially, a specific earthquake event is chosen, and input data is randomly selected (indicated by the blue line). We set virtual stations established at equidistant intervals from the epicenter, generate waveforms, and plot together with real observations. The red lines represent ground truth observations and black lines are the synthesized waveforms. Note that the azimuth angle of observations varies, while the synthetic stations are set to have same values. This potentially affect the P/S wave arrivals and lead to mismatch in visualization, but the effect is not considered to be significantly large.

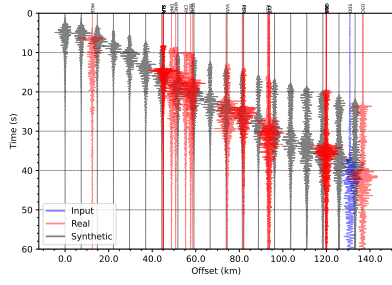


(a) Section plot on E axis

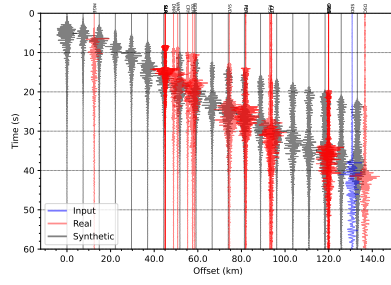
(b) Section plot on N axis

(c) Section plot on Z axis

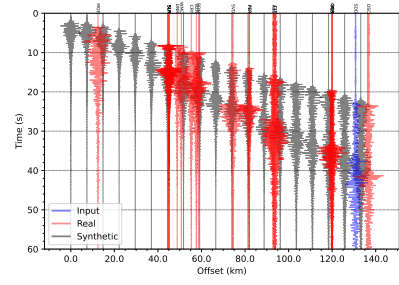
Figure 36: Section plot on synthetic stations.



(a) Section plot on E axis

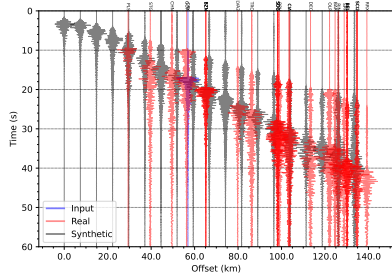


(b) Section plot on N axis

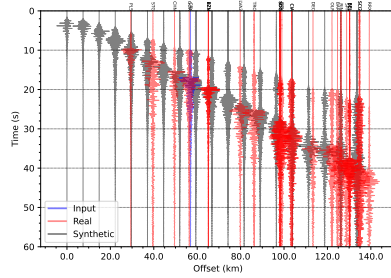


(c) Section plot on Z axis

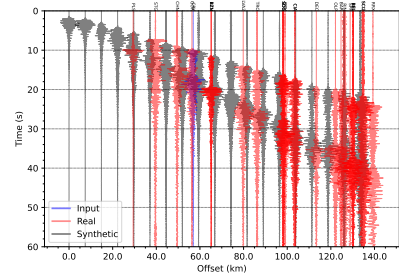
Figure 37: Section plot on synthetic stations.



(a) Section plot on E axis

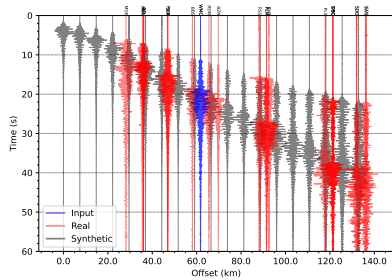


(b) Section plot on N axis

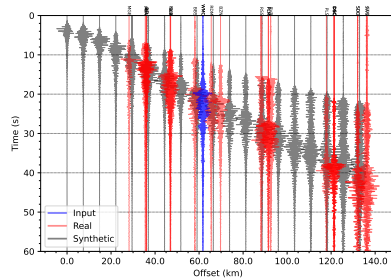


(c) Section plot on Z axis

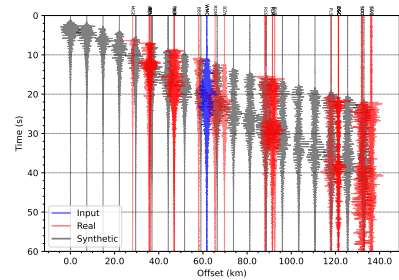
Figure 38: Section plot on synthetic stations.



(a) Section plot on E axis

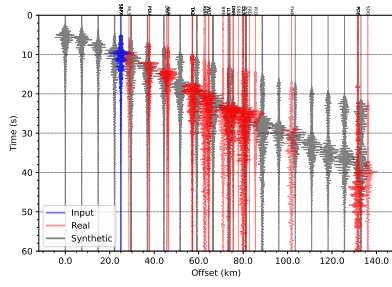


(b) Section plot on N axis

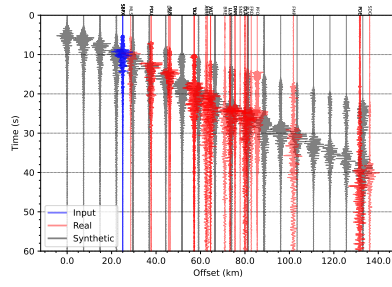


(c) Section plot on Z axis

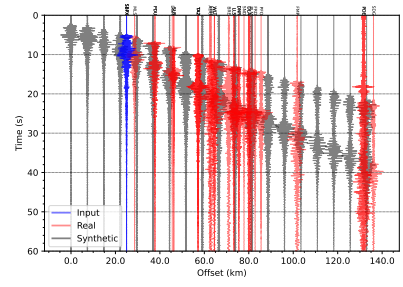
Figure 39: Section plot on synthetic stations.



(a) Section plot on E axis

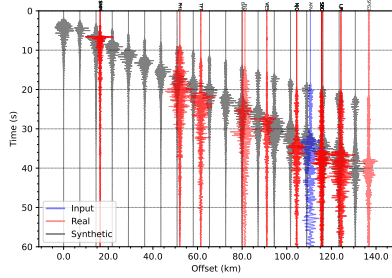


(b) Section plot on N axis

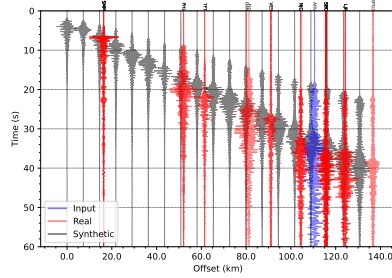


(c) Section plot on Z axis

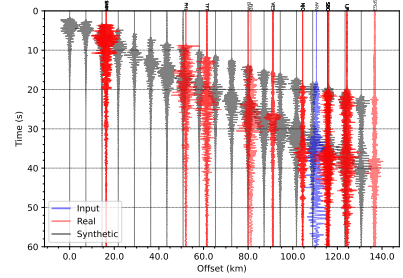
Figure 40: Section plot on synthetic stations.



(a) Section plot on E axis

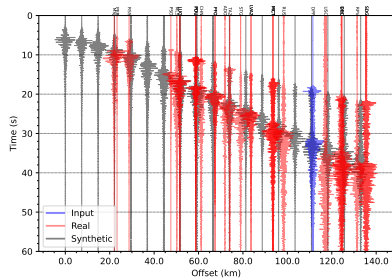


(b) Section plot on N axis

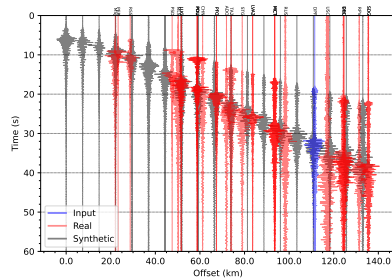


(c) Section plot on Z axis

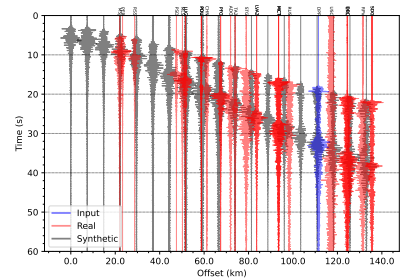
Figure 41: Section plot on synthetic stations.



(a) Section plot on E axis

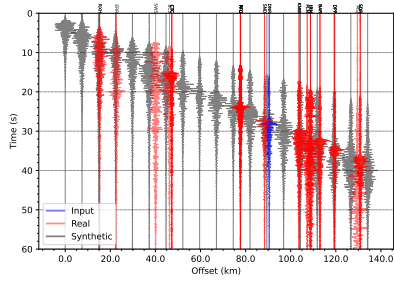


(b) Section plot on N axis

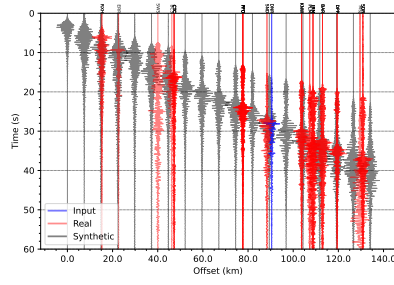


(c) Section plot on Z axis

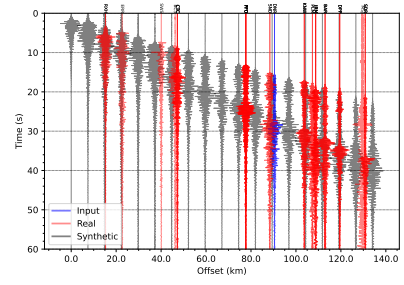
Figure 42: Section plot on synthetic stations.



(a) Section plot on E axis

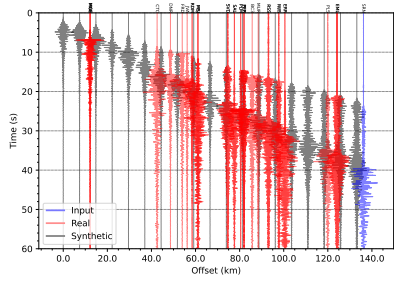


(b) Section plot on N axis

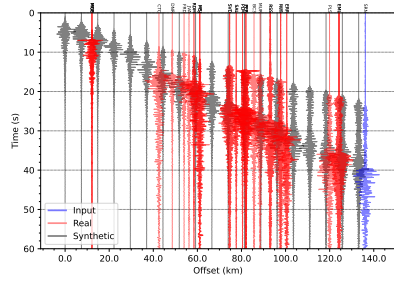


(c) Section plot on Z axis

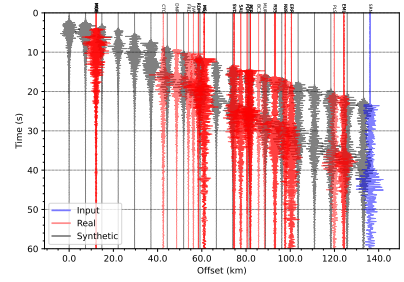
Figure 43: Section plot on synthetic stations.



(a) Section plot on E axis

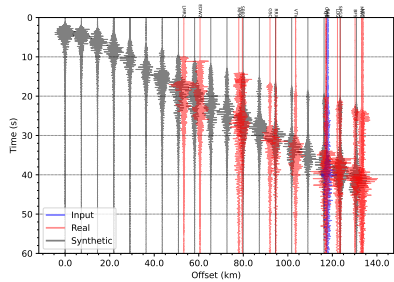


(b) Section plot on N axis

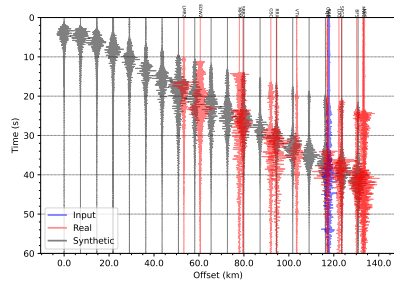


(c) Section plot on Z axis

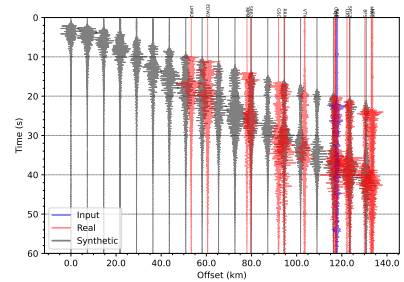
Figure 44: Section plot on synthetic stations.



(a) Section plot on E axis

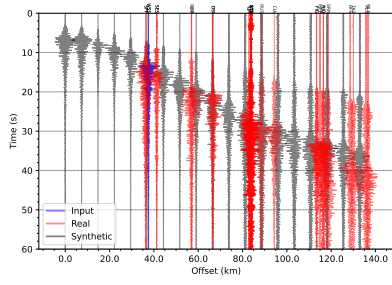


(b) Section plot on N axis

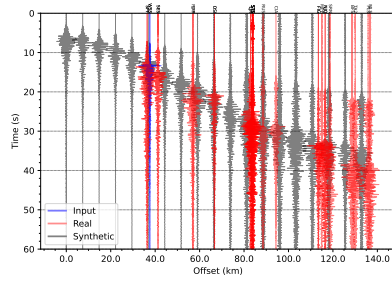


(c) Section plot on Z axis

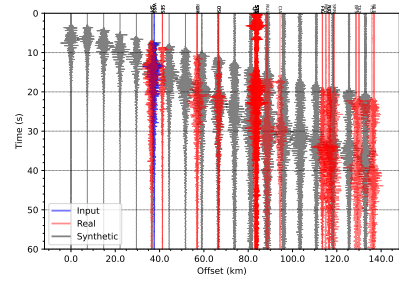
Figure 45: Section plot on synthetic stations.



(a) Section plot on E axis

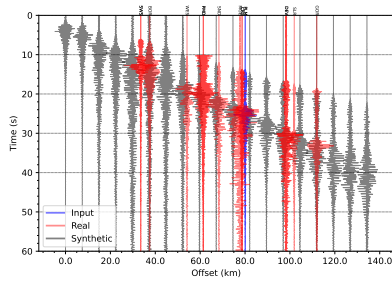


(b) Section plot on N axis

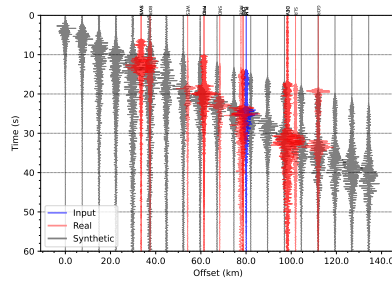


(c) Section plot on Z axis

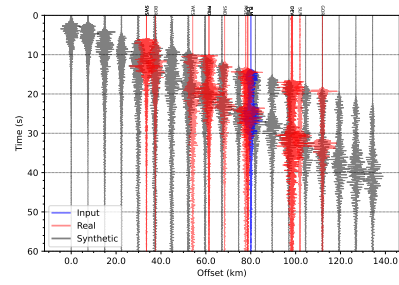
Figure 46: Section plot on synthetic stations.



(a) Section plot on E axis



(b) Section plot on N axis



(c) Section plot on Z axis

Figure 47: Section plot on synthetic stations.